

A conservative, physically compatible discretization for turbidity currents

Gonzalo de Diego^{a,b,*}, Marc Gerritsma^a, Artur Palha^a

^a*Delft University of Technology, Faculty of Aerospace Engineering*
^b*Oxford University*

Abstract

The recently introduced Mass Energy Enstrophy and Vorticity conserving (MEEVc) scheme for Navier-Stokes equations in 2D is extended to address turbidity currents. The structure preserving properties of the original scheme are preserved and a correct energy transfer is obtained for turbidity currents. The properties of the proposed discretization are proved and numerical results are presented. A comparison with literature results shows the ability of the new method to produce similar results with 10^2 less degrees of freedom.

Keywords: MEEVc, Turbidity currents, Structure preserving, Mimetic discretization

1. Introduction

1.1. Turbidity currents: introduction, relevance, and modelling approaches

Gravity currents are a general class of phenomena that are recurrent in science and engineering. Essentially, they are horizontally dominated flows originated by hydrostatic pressure gradients. This can be generically pictured as a fluid flowing within another fluid driven by the density difference between the two fluids. Specific cases of gravity currents are present in many situations, e.g.: tunnel fires, CO₂ sequestration in depleted oil reservoirs, snow avalanches, flow of molten steel on a horizontal surface, lava flows, haboobs (type of sandstorms), dorway flows, and turbidity currents (the focus of this work). For a detailed discussion of gravity currents see for example [1, 2], and [3, 4] for a more summarized introduction.

In the presence of suspended particles, it is frequent to have spatial variations in the bulk density of the fluid. In certain conditions, these variations of the bulk density generate pressure gradients, which induce gravity currents. Turbidity currents are a specific type of these particle-laden gravity currents where the interstitial fluid is a liquid (in most natural cases on Earth it is water) and the particles are typically small (e.g.: sand, clay, etc.) [5, 6]. They occur naturally in lakes and in oceans where they represent a fundamental process for sediment transport [7], since they contribute to both erosion and sedimentation [5]. The range of sediment transport by turbidity currents varies from a few hundreds of meters to thousands of kilometers [5, 6]. Besides their clear Geophysical interest, turbidity currents are very relevant from an Engineering point of view. First, because they are known to be an important contributor to the formation of deep sea oil reservoirs [8]. Second, due to their significant destructive power they are one of the main hazards to submarine telecommunication cables and pipelines [3, 9].

The study of turbidity currents is particularly challenging. *In situ* investigations are difficult since these particle-laden gravity currents are essentially unpredictable and their shear power typically destroys the measurement devices deployed to analyse them. Small-scale laboratory experiments are a good alternative that provides much understanding into the dynamics of turbidity currents. Unfortunately, they have limitations due to scaling constraints and existing measurement techniques [9, 10]. Another approach used in the study of gravity currents in general and turbidity currents in particular is modelling. Given the inherent multitude of flow regimes present in turbidity currents and depending on the particular aspects of interest in

*Corresponding author.

the flow, different modelling approaches may be used. These modelling approaches can be grouped into three fundamental types: (i) conceptual models, (ii) depth-averaged models, and (iii) depth-resolving models.

Conceptual models for the study of turbidity currents are mainly focussed on establishing analytical estimations (some very accurate) for the front velocity as a function of its height and excess density. These models date back to the seminal work of von Kármán, [11], which established the following relation for the Froude number, F_h ,

$$F_h = \frac{U}{\sqrt{g'h}} = \sqrt{\frac{2}{\sigma}}, \quad (1)$$

where U is the front velocity of the turbidity current, h represents its height, $g' := \frac{g(\rho_1 - \rho_2)}{\rho_1}$ stands for the reduced gravity, $\sigma := \frac{\rho_2}{\rho_1}$ corresponds to the density ratio, and as usual ρ_i is the density of the fluid i . Over the years, these models have become considerably more advanced and capable of addressing more general cases. For example, in the recent work by Konopliv et al., [12], a vorticity-based approach is extended to the case of non-Boussinesq gravity currents with success. Although very useful, these models give limited information into the flow and internal processes.

Depth-averaged models are a substantial step with regards to the provided insight into the internal dynamics of the flow of gravity currents. The most simple depth-averaged model available is the so called box model. In this approach the gravity current is modelled by a box (a rectangle in 2D, or a rectangular cuboid or cylinder in 3D) that can change its aspect ratio (stretch) as the flow evolves. Although a very simplified model, it can provide useful information on the dynamics of the front and of the height of the gravity current, especially how they are influenced by other parameters of the problem. For a detailed discussion of the box model see for example the monograph by Ungarish [2]. A more detailed depth-averaged representation of gravity currents can be achieved with shallow waters models. When the horizontal dimensions are much larger than the vertical one the shallow waters equations (depth-integrated Navier-Stokes equations) are a good approximation, see for example [13] for a derivation. Since the shallow waters equations provide a spatially dependent solution in the horizontal domain, it provides local values of velocity and height of the gravity current. Nevertheless, due to the strong assumptions on the invariance of the flow in the vertical direction this approximation has a limited scope of application and must be used with care in each specific case, as pointed out by Meiburg et al. [3]. For a more detailed discussion and further references see the works by Ungarish [2], and Meiburg et al. [3].

Depth-resolved models are the class of models that have the highest potential of providing accurate and detailed insights into the internal dynamics of the gravity currents, but they are also the most computationally expensive ones. These models solve the full Navier-Stokes equations describing the evolution of the gravity current. For this reason, the full three dimensional information can be retrieved from these models, with a level of detail dictated by the numerical approach used and the available computational resources. Depending on the specific case, different approximations can be used. For example, a Boussinesq approximation is relevant when the driving forces for the gravity current are small density variations; either an Eulerian-Lagrangian formulation tracking each individual particle or a fully Eulerian formulation may be used depending on the particles concentration and dimension. Given the typically high Reynolds numbers present in turbidity currents, a choice must be made regarding the level of detail with which turbulence is modelled. The three main options are (in increasing accuracy and computational cost): Reynolds Averaged Navier-Stokes (RANS), Large-Eddy Simulation (LES), and Direct Numerical Simulation (DNS). RANS equations are obtained by averaging the Navier-Stokes equations in time. Naturally, with this approach the output of these equations are the (temporal) mean fields. RANS simulations rely on a turbulence model that is highly dependent on problem specific parameters. For more details on RANS see Spalart [14] for a general introduction, and Meiburg et al. [3] for a summarised discussion focussing on gravity and turbidity currents. The LES formulation is more general and more accurate than RANS, but computationally more expensive. Contrary to RANS, LES relies on a grid dependent spatial filtering: all eddies up to a cutoff scale are resolved, and below this cutoff scale a subgrid-scale model is used to approximate the large scale effects of the small (unresolved) eddies. LES computations have the advantage of producing detailed time-dependent dynamics. For a detailed discussion of LES see Lesieur et al. [15] and Zhiyin [16], and Meiburg et al. [3] for a highlight on the aspects related to the simulation of turbidity currents. DNS directly solves

the Navier-Stokes equations fully resolving all scales (up to the dissipative Kolmogorov scale). Naturally, this requires very fine grids, which considerably limits the ability to model turbidity currents with very large Reynolds numbers. Nevertheless, the most detailed simulation can only be obtained by DNS simulations.

Early direct numerical simulations of gravity currents focused on the formation of intrusion fronts in lock exchange flows [17, 18]. The models used in these computations consist of the Boussinesq equation, in which a transport equation models the advection and diffusion of the density variable. Extensions to particle-laden flows were first carried out by Necker et al. [19, 20] with the equilibrium Eulerian approach. In these initial computations, the particle velocity field was assumed to be the sum of the carrier fluid’s velocity plus a constant settling velocity. Further studies have investigated gravity currents in more complex geometries [21, 22] and have considered non-Boussinesq flows [23]. Cantero et al. have extended the investigations on particle-laden flows and accounted for inertial effects, in addition to a settling velocity [24]. More recently, Parkinson et al. [9] have computed particle-laden flows with discontinuous Galerkin finite elements. Espath et al. [25] explore the validity of 2D computations of turbidity currents by comparing them with 3D computations and with experimental data. Meiburg et al. [3] make a thorough review of existing modelling approaches for gravity and turbidity currents and present very detailed 3D simulations, including interaction with obstacles.

In this work, we propose an energy conserving numerical discretization for turbidity currents based on an extension of the previously introduced Mass, Energy, Enstrophy, and Vorticity Conserving (MEEVC) scheme [26, 27]. Due to its conservation properties this method is capable of accurately representing the internal energy exchange and to accurately represent the evolution of fluid problem with a smaller number of degrees of freedom. Given its complexity, turbidity currents are a challenging test case for this numerical method. A more efficient numerical discretization can enable the simulation of larger and more complex flows. For the dilute-particle phase a simple approach is implemented: the equilibrium Eulerian method [28]. This new numerical scheme is assessed by simulating the lock exchange flow. Comparisons are made with existing results in order to evaluate the accuracy of the modified MEEVC scheme.

1.2. Overview of this work

In Section 2, a series of modelling possibilities for dilute particle-laden flows are presented, with special emphasis on the equilibrium Eulerian approach since is the one used in the work. Section 3 presents the lock exchange problem, specifying the required boundary conditions for modelling the settling of particles in turbidity currents. Next, in Section 4, the finite element discretization of the equilibrium Eulerian approach is presented. The energy budget of a turbidity current is examined in Section 5 in order to discuss the conservation properties of the solver. Finally, in Section 6, numerical results are presented for the lock exchange case and comparisons are made with the literature.

2. Modeling considerations

In this section, a series of modeling possibilities are presented for dilute suspensions. Of these, the equilibrium Eulerian model is chosen for the construction of the turbidity current solver and the equations of motion are derived.

2.1. Modeling approaches for dilute suspensions

A large set of modeling possibilities exist for particle-laden flows. The range of validity of these models is generally determined by two parameters: the Stokes number and the volumetric concentration of particles in the flow [29, 30]. The Stokes number is defined as the ratio τ_p/τ_f , where τ_p and τ_f are the characteristic time-scale of the particles and the smallest time-scale of the flow (i.e. the Kolmogorov time-scale), respectively. Assuming Stokes flow around the particles, τ_p can be calculated with,

$$\tau_p = \frac{\rho_p d^2}{18\rho_f \nu}, \quad (2)$$

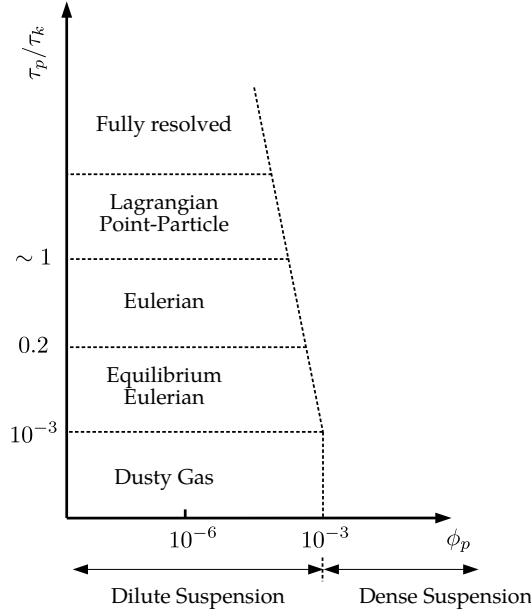


Figure 1: Different approaches to modeling particle-laden flows according to the volume fraction ϕ_p of the particle phase and time scale ratio (Stokes number). The inclined line reflects the increasing importance of particle collisions for larger particle sizes. Figure taken from Balachandar [30].

where ρ_p and ρ_f are the particle and fluid densities, respectively, d is the particle diameter and ν the dynamic viscosity of the fluid [29].

Figure 1 summarizes the modeling approaches for dilute particle suspensions. In this case, the volumetric concentration of particles is limited to $\phi_p < 10^{-3}$, such that a two-way coupling based on momentum exchange exists between the fluid and the particles. For higher concentrations, the flow is considered a dense suspension and particle-particle interaction becomes important (four-way coupling), [29].

The different modeling approaches indicated in Figure 1 are briefly explained below.

- **Dusty gas approach.** Particles are assumed to be sufficiently small such that they follow the carrier fluid. The equations to be solved are the Navier-Stokes equations with a modified density together with a transport equation for particles.
- **Equilibrium Eulerian approach.** Developed by Ferry and Balachandar and also known as the *fast Eulerian method* [28], this method retains the simplicity of the dusty gas approach by assuming that the particle velocity field can be expanded in terms of the carrier fluid velocity field and calculated by means of an algebraic equation. This method gives adequate results for particles with Stokes numbers just below unity and density ratio parameters ρ_p/ρ_f of order $\mathcal{O}(1)$ or lower. Further attention is given to this method in Section 2.2.
- **Eulerian approach.** Both the fluid and the particles are treated as two different continuum fluid phases. In this case, momentum and energy equations must also be solved for the particle phase. The principal restriction for this method is that within a small volume of fluid the particles must have a unique velocity, momentum and energy.
- **Lagrangian approach.** For $\tau_p/\tau_f > 1$, the relative particle sizes are such that the continuum phase assumption is no longer realistic, that is, assuming uniqueness of particle properties over small areas of the fluid is not valid. In the Lagrangian approach, particles are represented in a Lagrangian reference frame and their properties are calculated with probabilistic methods. In this case, there is

no requirement for uniqueness and the flow equations are valid until the Stokes number is such that the point-particle assumption no longer makes sense.

In this work, the equilibrium Eulerian approach will be used due to its simplicity and its capacity to capture both inertial and gravitational effects characteristic of turbidity currents. In the following subsection, the equilibrium assumption will be applied to the Eulerian-Eulerian equations and a set of equations for dilute suspensions will be derived.

2.2. Equilibrium Eulerian equations for a dilute suspension

A set of equations for a fluid-particle system studied from an Eulerian point of view can be obtained by mixture theory or by ensemble averaging [31]. The volumetric concentrations of the fluid and particle phases are denoted ϕ_f and ϕ_p respectively, the densities ρ_f and ρ_p and the velocities \vec{u}_p and \vec{u}_f .

By assuming constant densities for both phases and no mass transfer, the equations of motion in dimensional form can be written as follows [24],

$$\begin{cases} \frac{\partial \phi_f}{\partial t} + \nabla \cdot (\phi_f \vec{u}_f) = 0, \\ \frac{\partial \phi_p}{\partial t} + \nabla \cdot (\phi_p \vec{u}_p) = 0, \\ \phi_p \rho_p \frac{D_p \vec{u}_p}{Dt} = \phi_p (\rho_p - \rho_f) \vec{g} - \phi_d \nabla p + \vec{F}, \\ \phi_f \rho_f \frac{D_f \vec{u}_f}{Dt} = -\phi_f \nabla p + \mu \Delta \vec{u}_v - \vec{F}, \end{cases} \quad (3)$$

where \vec{F} represents the net hydrodynamic interaction between both phases, $\vec{g} = g\vec{e}_g$ is the gravitational acceleration vector (\vec{e}_g is the unit vector pointing in the direction of the gravitational force) and $\vec{u}_v = \phi_f \vec{u}_f + \phi_p \vec{u}_p$ is the composite velocity. D_f/Dt and D_p/Dt refer to the material derivatives following the fluid and particle velocity fields, respectively. The volume fractions satisfy the identity $\phi_f + \phi_p = 1$; hence, by adding the first two equations of (3),

$$\nabla \cdot \vec{u}_v = \nabla \cdot (\phi_f \vec{u}_f + \phi_p \vec{u}_p) = 0. \quad (4)$$

In the equilibrium Eulerian model, the velocity field of the particle phase, \vec{u}_p , is expanded about $\tau_p = 0$ and defined in terms of u_f . Given the density ratio parameter $\beta = 3/(2\rho_p/\rho_f + 1)$, for $\beta \sim \mathcal{O}(1)$, the following approximation holds up to $\mathcal{O}(\tau_p^{3/2})$:

$$\vec{u}_p \approx \vec{u}_f + \tau_p(1 - \beta) \left(\vec{g} - \frac{D_f \vec{u}_f}{Dt} \right), \quad (5)$$

For simplicity and to conform with existing computations [9, 19, 20, 25] for validation purposes, the inertial term of (5) is neglected, so that,

$$\vec{u}_p \approx \vec{u}_f + \tau_p(1 - \beta)\vec{g} = \vec{u}_f + u_s\vec{e}_g, \quad (6)$$

where $u_s = \tau_p(1 - \beta)g$ is the settling velocity of the particles.

The fact that the particle velocity field is completely defined by the velocity field of the carrier fluid leads to the following question: how will the initial particle distribution affect the resulting particle velocity field? It is possible to prove that, for sufficiently small particle sizes, an *equilibrium* particle field exists such that it depends only on fluid quantities [28]. In essence, this means that the transients arising from the initial conditions decay exponentially fast when the characteristic time-scale τ_p is much smaller than that of the fluid τ_f .

It is important to take into account that certain circumstances exist in which the Stokes number τ_p/τ_f is small but the equilibrium condition does not hold. An example is the injection of particles into a fluid

domain; near the point of injection, particle motion will be dominated by the injection process and only after an initial transient will it reach equilibrium with respect to the carrier fluid [30]. Furthermore, for increasing particle concentrations, the mean time between particle collisions will decrease until it reaches the particle response time τ_p and exerts a considerable effect on the particle velocity field.

Implicit in (6) is the assumption:

$$\frac{D_p \vec{u}_p}{Dt} \approx \frac{D_f \vec{u}_f}{Dt}. \quad (7)$$

Taking into account (7), the momentum equations in (3) can be combined in order to obtain

$$(\phi_f \rho_f + \phi_p \rho_p) \frac{D_f \vec{u}_f}{Dt} = -\nabla p + \mu \Delta \vec{u}_v + \phi_p (\rho_p - \rho_f) \vec{g}. \quad (8)$$

Considering that dilute suspensions are to be modeled and therefore $\phi_p \ll 1$, the composite velocity can be considered equal to the fluid velocity field, that is, $\vec{u}_v \approx \vec{u}_f$. By using (4), the conservation of mass for the fluid phase can be described with a divergence-free constraint,

$$\nabla \cdot \vec{u}_f \approx 0. \quad (9)$$

Finally, the Boussinesq approximation is assumed to hold, such that density variations are considered to be small and only influence the buoyancy term of (8). The density term on the left-hand side of (8) is assumed constant, such that $(\phi_f \rho_f + \phi_p \rho_p) \approx \rho_f$. In order to write the simplified equations of motion in non-dimensional form, a characteristic velocity, length and density are defined. The characteristic density is taken as ρ_f and, when considering a lock exchange flow, the characteristic length is taken as the height of the channel, H , see Figure 2. The buoyancy velocity, defined as

$$u_b = \sqrt{gH \frac{\rho_p - \rho_f}{\rho_f} \phi_{p,\max}}, \quad (10)$$

is used as the characteristic velocity. $\phi_{p,\max}$ represents the maximum volumetric concentration of particles in the domain at the initial time instant. For simplicity of notation, the non-dimensional fluid velocity, \vec{u}_f will be represented with \vec{u} and the variable $\phi = \phi_p / \phi_{p,\max}$ will be used as a normalized measure of particle concentration. The non-dimensional equations of motion are given by,

$$\begin{cases} \nabla \cdot \vec{u} = 0, \\ \frac{\partial \vec{u}}{\partial t} + (\vec{u} \cdot \nabla) \vec{u} = -\nabla p + \frac{1}{\sqrt{\text{Gr}}} \Delta \vec{u} + \phi \vec{e}_g, \\ \frac{\partial \phi}{\partial t} + (\vec{u} + u_s \vec{e}_g) \cdot \nabla \phi = \frac{1}{\sqrt{\text{GrSc}^2}} \Delta \phi. \end{cases} \quad (11)$$

In Equation (11), a diffusion term has been added to the equation for conservation of particles. This is common practice when considering particle-laden flows, as it avoids the formation of sharp concentrations of particles that could lead to numerical instabilities [19, 20, 24]. Furthermore, certain authors indicate that this term has a physical significance, such as the spreading of particles in time due to hydrodynamic diffusion [20] or the departure of the equilibrium assumption due to close interaction of particles [24].

The two non-dimensional parameters that appear in (11) are the Grashof number Gr and the Schmidt number Sc , defined by

$$\text{Gr} = \left(\frac{u_b H}{\nu} \right)^2 \quad \text{and} \quad \text{Sc} = \frac{\nu}{\kappa}. \quad (12)$$

The Grashof number represents the ratio of buoyancy forces and viscous forces and it is proportional to Re^2 . The Schmidt number compares the viscous diffusivity of the fluid to the molecular diffusivity of the particle field, given by κ .

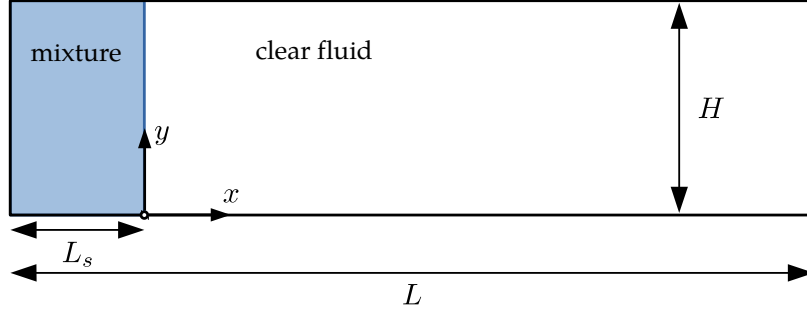


Figure 2: Initial set-up of the lock-exchange test-case to be computed in this work.

3. The 2D lock exchange flow

In this section, the 2D lock-exchange flow problem of a particle-driven current is presented together with the boundary conditions that will be prescribed in order to capture the deposition of sediment along the lower boundary. A lock-exchange flow consists of the mutual propagation of two flows with different densities which were initially separated by a membrane. Many physically relevant features of gravity currents can be observed in this type of flow, such as the body-head structure that gradually develops as the flow evolves [17, 18, 24]. Extensive experimental studies have been carried out with lock-exchange flows [32]; more recently, direct numerical simulations have been used in order to capture more subtle physical aspects of the flow or to test numerical solvers for gravity currents [9, 17–19, 21–25].

The initial set-up of the lock-exchange flow computed in this work is shown in Figure 2 and corresponds to the one presented by Necker et al. [19] and used in the work of Parkinson et al. [9] and Espath et al. [25]. The domain consists in a plane channel of height H and length L . At $t = 0$, a mixture of the particle phase and the fluid phase is contained in the region $[-L_s, 0] \times [0, H]$. For $t > 0$, the mixture is put in touch with the clear fluid and an intrusion front develops as the heavier fluid propagates along the lower boundary.

3.1. Boundary conditions

In order to solve (11), boundary conditions must be given for the velocity \vec{u} and particle concentration ϕ . Boundary conditions will be prescribed in the same way as Espath et al. [25], such that the lower wall allows for the convection of the flow particles at a settling velocity u_s . To this end, the boundary $\partial\Omega$ is partitioned into 4 regions which correspond with the 4 faces of the rectangle, such that $\partial\Omega = \cup \Gamma_i$, for $i = 1, 2, 3$ and 4, see Figure 3.

The velocity boundary conditions consist of no-slip conditions along the upper and lower walls, such that

$$\vec{u} = 0 \quad \text{on } \Gamma_1 \cup \Gamma_3, \quad (13)$$

and shear free conditions with no penetration along the lateral walls,

$$\vec{u} \cdot \vec{n} = 0 \quad \text{and} \quad \nabla \vec{u} \cdot \vec{n} = 0 \quad \text{on } \Gamma_2 \cup \Gamma_4. \quad (14)$$

Taking into account that (11) will be solved in a (\vec{u}, ω, p) formulation, the shear-free boundary conditions can also be written in the following form,

$$\vec{u} \cdot \vec{n} = 0 \quad \text{and} \quad \omega = 0 \quad \text{on } \Gamma_2 \cup \Gamma_4. \quad (15)$$

A fundamental feature of turbidity currents is the deposition and resuspension of particles, which modifies the driving force of the current [24]. For the lock exchange flow, deposition of particles is assumed to occur on the lower boundary, Γ_3 , due to advection with $u_s \vec{e}_g$. Over $\Gamma_1 \cup \Gamma_2 \cup \Gamma_4$, no particle transport is assumed to hold.

$$\begin{array}{l}
\Gamma_1 : \vec{u} = 0 \text{ and } -u_s \phi \vec{e}_g \cdot \vec{n} + \frac{1}{\sqrt{\text{GrSc}^2}} \nabla \phi \cdot \vec{n} = 0 \\
\hline
\begin{array}{ll}
\Gamma_2 : & \Gamma_4 : \\
\vec{u} \cdot \vec{n} = 0, & \vec{u} \cdot \vec{n} = 0, \\
\omega = 0 \text{ and} & \omega = 0 \text{ and} \\
\nabla \phi \cdot \vec{n} = 0 & \nabla \phi \cdot \vec{n} = 0
\end{array} \\
\hline
\Gamma_3 : \vec{u} = 0 \text{ and } \nabla \phi \cdot \vec{n} = 0
\end{array}$$

Figure 3: Boundary conditions for the lock exchange test-case.

In order to understand how these boundary conditions can be prescribed, the transport equation for ϕ must be integrated over the domain Ω . Taking into account that $\nabla \cdot \vec{u} = 0$ in Ω and $\vec{u} \cdot \vec{n} = 0$ on $\partial\Omega$, integrating the particle transport equation in (11) over Ω yields the following result after applying the divergence theorem,

$$\frac{d}{dt} \int_{\Omega} \phi \, d\Omega = \int_{\partial\Omega} \left(-\phi u_s \vec{e}_g + \frac{1}{\sqrt{\text{GrSc}^2}} \nabla \phi \right) \cdot \vec{n} \, d\Gamma. \quad (16)$$

Therefore, if the boundary condition for ϕ on $\Gamma_1 \cup \Gamma_2 \cup \Gamma_4$ is zero particle flux, the integral in Equation (16) must be equal to zero, such that

$$\left(-\phi u_s \vec{e}_g + \frac{1}{\sqrt{\text{GrSc}^2}} \nabla \phi \right) \cdot \vec{n} = 0 \quad \text{on } \Gamma_1 \cup \Gamma_2 \cup \Gamma_4. \quad (17)$$

If the gravity vector is set to $\vec{e}_g = (0, -1)$, the following boundary conditions hold:

$$\begin{cases} -u_s \phi \vec{e}_g \cdot \vec{n} + \frac{1}{\sqrt{\text{GrSc}^2}} \nabla \phi \cdot \vec{n} = 0 & \text{on } \Gamma_1, \\ \nabla \phi \cdot \vec{n} = 0 & \text{on } \Gamma_2 \cup \Gamma_4. \end{cases} \quad (18)$$

Deposition of particles is enabled by assuming that the boundary condition over Γ_2 is a particle flux at a velocity u_s . In order to do so, the dissipation term in (16) is eliminated, such that

$$\nabla \phi \cdot \vec{n} = 0 \quad \text{on } \Gamma_3. \quad (19)$$

Therefore, given the boundary conditions (18) and (19), the variation of the total particle concentration is determined with the following expression,

$$\frac{d}{dt} \int_{\Omega} \phi \, d\Omega = - \int_{\Gamma_3} \phi u_s \, d\Gamma. \quad (20)$$

4. Numerical discretization

In this work we introduce a structure preserving discretization for turbidity currents based on the MEEVC discretization, [26, 27]. We start by briefly introducing the MEEVC discretization for a homogeneous fluid first for case of periodic boundaries and then for the case of non-periodic boundary conditions. The MEEVC method will be presented on an *ad hoc* basis, for a detailed discussion on the construction of the method and proof of its properties the reader is directed to [26, 27]. Once the MEEVC method for a homogeneous fluid has been presented the extension to turbidity currents will be discussed in detail.

4.1. Brief introduction to the MEEVC discretization

4.1.1. Spatial discretization (periodic boundary conditions)

The most common form of the Navier-Stokes equations for 2D viscous incompressible flows, as seen above, is expressed as a set of conservation laws for momentum and mass involving the velocity $\vec{u} : \Omega \times (0, t_F] \mapsto \mathbb{R}^2$ and pressure $p : \Omega \times (0, t_F] \mapsto \mathbb{R}$:

$$\begin{cases} \frac{\partial \vec{u}}{\partial t} + (\vec{u} \cdot \nabla) \vec{u} + \nabla p = \nu \Delta \vec{u} + \vec{s}, & \text{in } \Omega \times (0, t_F], \\ \nabla \cdot \vec{u} = 0, & \text{in } \Omega \times (0, t_F], \end{cases} \quad (21)$$

with the final time instant $t_F > 0$, ν the kinematic viscosity, \vec{s} the body force per unit mass, and $\Delta = \nabla \cdot \nabla$ the Laplace operator. These equations are valid on the fluid domain Ω , together with suitable initial and boundary conditions. At this stage, we consider only periodic boundary conditions and we set $\vec{s} = 0$.

The form of the Navier-Stokes equations presented in (21) is the so called *convective form*. Its name stems from the particular form of the nonlinear term $(\vec{u} \cdot \nabla) \vec{u}$, which underlines its convective nature. This form is not unique. Using well known vector calculus identities it is possible to rewrite the nonlinear term in three other forms: *divergence form*, *skew-symmetric form*, and *rotational form* (see for example Zang [33], Morinishi [34], and Rønquist [35]).

The MEEVC discretization uses as a starting point the *rotational form*, which makes use of the vorticity $\omega := \nabla \times \vec{u}$:

$$\begin{cases} \frac{\partial \vec{u}}{\partial t} + \omega \times \vec{u} + \nabla \bar{p} = \nu \Delta \vec{u}, & \text{in } \Omega \times (0, t_F], \\ \nabla \cdot \vec{u} = 0, & \text{in } \Omega \times (0, t_F], \end{cases} \quad (22)$$

where the static pressure p is replaced by the total pressure $\bar{p} := \frac{1}{2} \vec{u} \cdot \vec{u} + p$.

By introducing an unknown, the vorticity, we lack one additional equation in order to close the system. Different options could be used (each with its advantages and drawbacks): (i) $\omega := \nabla \times \vec{u}$ (kinematic equation), (ii) $\Delta \psi = \omega$ with $\nabla \times \psi = \vec{u}$ (stream function), and (iii) a dynamic equation for vorticity. In the MEEVC method the third route is followed.

It is well known that by taking the curl of the momentum equation and using the kinematic definition $\omega := \nabla \times \vec{u}$ we can obtain the flow equations based on vorticity transport:

$$\begin{cases} \frac{\partial \omega}{\partial t} + \frac{1}{2} (\vec{u} \cdot \nabla) \omega + \frac{1}{2} \nabla \cdot (\vec{u} \omega) = \nu \Delta \omega, & \text{in } \Omega \times (0, t_F], \\ \nabla \cdot \vec{u} = 0, & \text{in } \Omega \times (0, t_F], \\ \omega = \nabla \times \vec{u}, & \text{in } \Omega \times (0, t_F]. \end{cases} \quad (23)$$

This velocity-vorticity (\vec{u}, ω) formulation of the Navier-Stokes equations is of particular interest for vortex dominated flows, see for example Gatski [36] for an overview and Daube [37] and Clercx [38] for applications.

The MEEVC discretization starts with a (\vec{u}, ω) formulation by combining the rotational form (22) with the vorticity transport equation (23):

$$\begin{cases} \frac{\partial \vec{u}}{\partial t} + \omega \times \vec{u} + \nabla \bar{p} = -\nu \nabla \times \omega, & \text{in } \Omega \times (0, t_F], \\ \frac{\partial \omega}{\partial t} + \frac{1}{2} (\vec{u} \cdot \nabla) \omega + \frac{1}{2} \nabla \cdot (\vec{u} \omega) = \nu \Delta \omega, & \text{in } \Omega \times (0, t_F], \\ \nabla \cdot \vec{u} = 0 & \text{in } \Omega \times (0, t_F]. \end{cases} \quad (24)$$

An important aspect we wish to stress is that although at the continuous level the kinematic definition $\omega := \nabla \times \vec{u}$ is exactly satisfied, at the discrete level it is not always guaranteed that this identity holds exactly. In fact, in the discretization presented here this identity is satisfied only approximately. This, as can be seen in [26, 27], enables the construction of a mass, energy, enstrophy and vorticity conserving discretization (MEEVC).

The next step for developing the MEEVC discretization is the construction of the weak form of (24), as is standard in finite elements:

$$\left\{ \begin{array}{l} \text{Find } \vec{u} \in H(\text{div}, \Omega), \bar{p} \in L^2(\Omega) \text{ and } \omega \in H(\text{curl}, \Omega) \text{ such that:} \\ \langle \frac{\partial \vec{u}}{\partial t}, \vec{v} \rangle_\Omega + \langle \omega \times \vec{u}, \vec{v} \rangle_\Omega - \langle \bar{p}, \nabla \cdot \vec{v} \rangle_\Omega = -\nu \langle \nabla \times \omega, \vec{v} \rangle_\Omega, \quad \forall \vec{v} \in H(\text{div}, \Omega), \\ \langle \frac{\partial \omega}{\partial t}, \xi \rangle_\Omega - \frac{1}{2} \langle \omega, \nabla \cdot (\vec{u} \xi) \rangle_\Omega + \frac{1}{2} \langle \nabla \cdot (\vec{u} \omega), \xi \rangle_\Omega = \nu \langle \nabla \times \omega, \nabla \times \xi \rangle_\Omega, \quad \forall \xi \in H(\text{curl}, \Omega), \\ \langle \nabla \cdot \vec{u}, q \rangle_\Omega = 0, \quad \forall q \in L^2(\Omega), \end{array} \right. \quad (25)$$

where we have used integration by parts and the periodic boundary conditions to obtain the identities $\langle \bar{p}, \nabla \cdot \vec{v} \rangle_\Omega = -\langle \nabla \bar{p}, \vec{v} \rangle_\Omega$, $\langle \omega, \nabla \cdot (\vec{u} \xi) \rangle_\Omega = -\langle (\vec{u} \cdot \nabla) \omega, \xi \rangle_\Omega$ and $\langle \nabla \times \omega, \nabla \times \xi \rangle_\Omega = \langle \Delta \omega, \xi \rangle_\Omega$. The space $L^2(\Omega)$ corresponds to square integrable functions and the spaces $H(\text{div}, \Omega)$ and $H(\text{curl}, \Omega)$ contain square integrable functions whose divergence and curl are also square integrable.

The crucial step to transform these finite dimensional continuous equations into computable finite dimensional equations relies on a choice of adequate conforming finite dimensional function spaces, where we will seek our discrete solutions for velocity \vec{u}_h , pressure \bar{p}_h and vorticity ω_h :

$$\vec{u}_h \in U_h \subset H(\text{div}, \Omega), \quad \bar{p}_h \in Q_h \subset L^2(\Omega) \quad \text{and} \quad \omega_h \in W_h \subset H(\text{curl}, \Omega). \quad (26)$$

As usual, each of these finite dimensional function spaces, U_h , Q_h and W_h , has an associated finite set of basis functions, $\vec{\epsilon}_i^U$, ϵ_i^Q , ϵ_i^W , such that

$$U_h = \text{span}\{\vec{\epsilon}_1^U, \dots, \vec{\epsilon}_{d_U}^U\}, \quad Q_h = \text{span}\{\epsilon_1^Q, \dots, \epsilon_{d_Q}^Q\} \quad \text{and} \quad W_h = \text{span}\{\epsilon_1^W, \dots, \epsilon_{d_W}^W\}, \quad (27)$$

where d_U , d_Q and d_W denote the dimension of the discrete function spaces and therefore correspond to the number of degrees of freedom for each of the unknowns. As a consequence, the approximate solutions for velocity, pressure and vorticity can be expressed as a linear combination of these basis functions

$$\vec{u}_h := \sum_{i=1}^{d_U} u_i \vec{\epsilon}_i^U, \quad \bar{p}_h := \sum_{i=1}^{d_Q} p_i \epsilon_i^Q \quad \text{and} \quad \omega_h := \sum_{i=1}^{d_W} \omega_i \epsilon_i^W, \quad (28)$$

with u_i , p_i and ω_i the degrees of freedom of velocity, total pressure and vorticity, respectively. Since the Navier-Stokes equations form a time dependent set of equations, in general these coefficients will be time dependent, $u_i = u_i(t)$, $p_i = p_i(t)$ and $\omega_i = \omega_i(t)$.

The choice of the finite dimensional function spaces dictates the properties of the discretization. In order to have exact conservation of mass, energy, enstrophy, and total vorticity we must choose these function spaces such that they form a Hilbert subcomplex

$$0 \longrightarrow W_h \xrightarrow{\nabla \times} U_h \xrightarrow{\nabla \cdot} Q_h \longrightarrow 0, \quad (29)$$

that mimics the 2D Hilbert complex associated to the continuous functional spaces:

$$0 \longrightarrow H(\text{curl}, \Omega) \xrightarrow{\nabla \times} H(\text{div}, \Omega) \xrightarrow{\nabla \cdot} L^2(\Omega) \longrightarrow 0. \quad (30)$$

The Hilbert complex is an important structure that is intimately related to the de Rham complex of differential forms. The construction of a discrete subcomplex is an important requirement to obtain stable and accurate finite element discretizations, see for example [39–45] for a general discussion and [26] for the specific discussion on the MEEVC formulation.

One specific choice of discrete function spaces is

$$W_h = \text{CG}_N, \quad U_h = \text{RT}_N, \quad \text{and} \quad Q_h = \text{DG}_{N-1}, \quad (31)$$

where CG_N are the Lagrange elements of degree N , see [46], RT_N are the Raviart-Thomas elements of degree N , see [46, 47], and DG_{N-1} are the discontinuous Lagrange elements of degree $(N-1)$, see [46].

Using the discrete expansions for \vec{u}_h , \vec{p}_h and ω_h , (28), can be transformed into its discrete counterpart

$$\left\{ \begin{array}{l} \text{Find } \mathbf{u} \in \mathbb{R}^{d_U}, \bar{\mathbf{p}} \in \mathbb{R}^{d_Q} \text{ and } \boldsymbol{\omega} \in \mathbb{R}^{d_W} \text{ such that:} \\ \sum_{i=1}^{d_U} \frac{du_i}{dt} \langle \vec{\epsilon}_i^U, \vec{\epsilon}_j^U \rangle_\Omega + \sum_{i=1}^{d_U} u_i \langle \omega_h \times \vec{\epsilon}_i^U, \vec{\epsilon}_j^U \rangle_\Omega - \sum_{k=1}^{d_Q} p_k \langle \epsilon_k^Q, \nabla \cdot \vec{\epsilon}_j^U \rangle_\Omega = -\nu \langle \nabla \times \omega_h, \vec{\epsilon}_j^U \rangle_\Omega, \quad j = 1, \dots, d_U, \\ \sum_{i=1}^{d_W} \frac{d\omega_i}{dt} \langle \epsilon_i^W, \epsilon_j^W \rangle_\Omega - \sum_{i=1}^{d_W} \frac{\omega_i}{2} \langle \epsilon_i^W, \nabla \cdot (\vec{u}_h \epsilon_j^W) \rangle_\Omega + \sum_{i=1}^{d_W} \frac{\omega_i}{2} \langle \nabla \cdot (\vec{u}_h \epsilon_i^W), \epsilon_j^W \rangle_\Omega = \nu \sum_{i=1}^{d_W} \omega_i \langle \nabla \times \epsilon_i^W, \nabla \times \epsilon_j^W \rangle_\Omega, \quad j = 1, \dots, d_W, \\ \sum_{i=1}^{d_U} u_i \langle \nabla \cdot \vec{\epsilon}_i^U, \epsilon_j^Q \rangle_\Omega = 0, \quad j = 1, \dots, d_Q, \end{array} \right. \quad (32)$$

with $\mathbf{u} := [u_1, \dots, u_{d_U}]^\top$, $\bar{\mathbf{p}} := [p_1, \dots, p_{d_Q}]^\top$ and $\boldsymbol{\omega} := [\omega_1, \dots, \omega_{d_W}]^\top$. Using matrix notation, (32) can be expressed more compactly as

$$\left\{ \begin{array}{l} \text{Find } \mathbf{u} \in \mathbb{R}^{d_U}, \bar{\mathbf{p}} \in \mathbb{R}^{d_Q} \text{ and } \boldsymbol{\omega} \in \mathbb{R}^{d_W} \text{ such that:} \\ \mathbf{M} \frac{d\mathbf{u}}{dt} + \mathbf{R} \mathbf{u} - \mathbf{P} \bar{\mathbf{p}} = -\nu \mathbf{l}, \\ \mathbf{N} \frac{d\boldsymbol{\omega}}{dt} - \frac{1}{2} \mathbf{W} \boldsymbol{\omega} + \frac{1}{2} \mathbf{W}^\top \boldsymbol{\omega} = \nu \mathbf{L} \boldsymbol{\omega}, \\ \mathbf{D} \mathbf{u} = 0, \end{array} \right. \quad (33)$$

The coefficients of the matrices \mathbf{M} , \mathbf{R} and \mathbf{P} , and the column vector \mathbf{l} are given by

$$\mathbf{M}_{ij} := \langle \vec{\epsilon}_j^U, \vec{\epsilon}_i^U \rangle_\Omega, \quad \mathbf{R}_{ij} := \langle \omega_h \times \vec{\epsilon}_j^U, \vec{\epsilon}_i^U \rangle_\Omega, \quad \mathbf{P}_{ij} := \langle \epsilon_j^Q, \nabla \cdot \vec{\epsilon}_i^U \rangle_\Omega \quad \text{and} \quad l_i := \langle \nabla \times \omega_h, \vec{\epsilon}_i^U \rangle_\Omega. \quad (34)$$

Similarly, the coefficients of the matrices \mathbf{N} , \mathbf{W} , \mathbf{L} and \mathbf{D} are given by

$$\mathbf{N}_{ij} := \langle \epsilon_j^W, \epsilon_i^W \rangle_\Omega, \quad \mathbf{W}_{ij} := \langle \epsilon_j^W, \nabla \cdot (\vec{u}_h \epsilon_i^W) \rangle_\Omega, \quad \mathbf{L}_{ij} := \langle \nabla \times \epsilon_j^W, \nabla \times \epsilon_i^W \rangle_\Omega \quad \text{and} \quad \mathbf{D}_{ij} := \langle \nabla \cdot \vec{\epsilon}_j^U, \epsilon_i^Q \rangle_\Omega. \quad (35)$$

4.1.2. Temporal discretization (periodic boundary conditions)

Once the spatial discretization is introduced we end up with a set of ordinary differential equations, (33). The main objective that drives the choice of the time discretization for (33) is preservation of invariants: mass, energy, enstrophy, and total vorticity. Not all time integrators satisfy these invariance properties and therefore will spoil all properties obtained so far with the spatial discretization. For the MEEVC scheme the lowest order Gauss time integrator, $s = 1$, also known as the *midpoint rule*, because it enables the construction of an explicit staggered integrator in time. For more details on Gauss time integrators see [48].

When applied to the solution of a 1D ordinary differential equation of the form

$$\left\{ \begin{array}{l} \frac{df}{dt} = g(f(t), t), \\ f(0) = f_0, \end{array} \right. \quad (36)$$

the one stage Gauss integrator results in the following implicit time stepping scheme

$$\frac{f^k - f^{k-1}}{\Delta t} = g\left(\frac{f^k + f^{k-1}}{2}, t + \frac{\Delta t}{2}\right), \quad k = 1, \dots, M, \quad (37)$$

where $f^0 = f_0$, Δt is the time step and M is the number of time steps. The direct application of (37) to the discrete weak form (33) results in a fully implicit scheme. This means that the resulting system of equations

is a fully coupled set of nonlinear equations, which requires a computationally expensive iterative procedure to solve. To circumvent this penalty, instead of defining all the unknown physical quantities \vec{u}_h , ω_h and \bar{p}_h , at the same time instants t^k we choose to stagger them in time. In this way it is possible to obtain two systems of quasi-linear equations. The unknown vorticity and total pressure are defined at the integer time instants ω_h^k , \bar{p}_h^k and the unknown velocity is defined at the intermediate time instants $\vec{u}_h^{k+\frac{1}{2}}$, see Figure 4. Taking into account this staggered approach, the fully discrete counterpart of (33) can be rewritten as

$$\begin{cases} \text{Find } \mathbf{u}_h^{k+\frac{3}{2}} \in \mathbb{R}^{d_U}, \bar{\mathbf{p}}^{k+1} \in \mathbb{R}^{d_Q} \text{ and } \boldsymbol{\omega}^{k+1} \in \mathbb{R}^{d_W} \text{ such that:} \\ \mathbf{M} \frac{\mathbf{u}_h^{k+\frac{3}{2}} - \mathbf{u}_h^{k+\frac{1}{2}}}{\Delta t} + \mathbf{R}^{k+1} \frac{\mathbf{u}_h^{k+\frac{3}{2}} + \mathbf{u}_h^{k+\frac{1}{2}}}{2} - \mathbf{P} \bar{\mathbf{p}}^{k+1} = -\nu \mathbf{l}^{k+1}, \\ \mathbf{N} \frac{\boldsymbol{\omega}^{k+1} - \boldsymbol{\omega}^k}{\Delta t} - \frac{1}{2} \mathbf{W}^{k+\frac{1}{2}} \frac{\boldsymbol{\omega}^{k+1} + \boldsymbol{\omega}^k}{2} + \frac{1}{2} \left(\mathbf{W}^{k+\frac{1}{2}} \right)^\top \frac{\boldsymbol{\omega}^{k+1} + \boldsymbol{\omega}^k}{2} = \nu \mathbf{L} \frac{\boldsymbol{\omega}^{k+1} + \boldsymbol{\omega}^k}{2}, \\ \mathbf{D} \mathbf{u}_h^{k+\frac{3}{2}} = 0, \end{cases} \quad (38)$$

where, for compactness of notation, we have set

$$\tilde{\mathbf{u}}_h^{k+\frac{1}{2}} := \frac{\vec{u}_h^{k+1} + \vec{u}_h^k}{2} \quad \text{and} \quad \tilde{\omega}_h^{k+\frac{1}{2}} := \frac{\omega_h^{k+1} + \omega_h^k}{2}. \quad (39)$$

Note that $\vec{u}_h^{k+\frac{1}{2}}$ and ω_h^k are known at the start of each time step. All matrix operators are as in (34) and (35), with the exception of \mathbf{R}^{k+1} , $\mathbf{W}^{k+\frac{1}{2}}$ and \mathbf{l}^{k+1} , the coefficients of which are

$$\mathbf{R}_{ij}^{k+1} := \langle \omega_h^{k+1} \times \vec{e}_j^U, \vec{e}_i^U \rangle_\Omega, \quad \mathbf{l}_i^{k+1} := \langle \nabla \times \omega_h^{k+1}, \vec{e}_i^U \rangle_\Omega \quad \text{and} \quad \mathbf{W}_{ij}^{k+\frac{1}{2}} := \langle \epsilon_j^W, \nabla \cdot (\vec{u}_h^{k+\frac{1}{2}} \epsilon_i^W) \rangle_\Omega. \quad (40)$$

To start the iteration procedure $\vec{u}_h^{\frac{1}{2}}$ and ω_h^0 are required. Since only \vec{u}_h^0 and ω_h^0 are known, the first time step needs to be implicit. The remaining time steps can then be computed explicitly with (38).

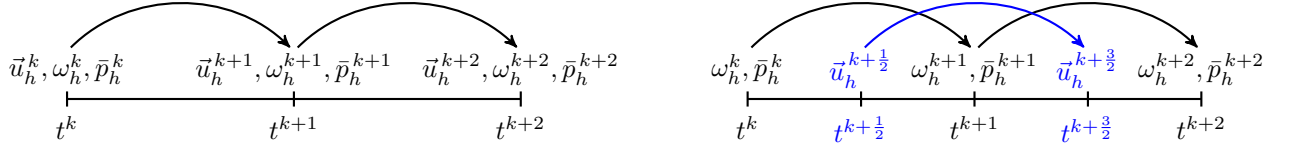


Figure 4: Diagram of the time stepping. Left: all unknowns at the same time instant, as in (33) Right: staggered in time unknowns, as in (38).

4.1.3. Full discretization (non-periodic boundary conditions)

In general, functions in $H(\text{div}, \Omega)$ -conforming finite element spaces like the Raviart-Thomas elements satisfy weaker continuity requirements than functions contained in $(H^1(\Omega))^2$ -conforming spaces, like continuous Galerkin vector elements. In particular, the degrees of freedom of the Raviart-Thomas finite element are calculated in terms of moments of the normal components of the vector along the faces of the cell [46, 49]. As a result, one has no control over the tangential component along a face of functions in this space. It follows that tangential boundary conditions cannot be imposed strongly.

This problem was considered in [27] and three solutions were suggested which consisted in imposing vorticity boundary conditions on the vorticity transport equation. Of these 3 methods, the kinematic Neumann vorticity boundary condition was shown to yield the best approximations and therefore only this method will be considered here. Basically, an additional vorticity $\tilde{\omega}$ is introduced and calculated by means of the kinematic relation $\tilde{\omega} = \nabla \times \vec{u}$ together with the tangential velocity boundary condition. Then, when solving the vorticity transport equation, the boundary condition $\nabla \times \omega \times \vec{n} = \nabla \times \tilde{\omega} \times \vec{n}$ on $\partial\Omega$ is imposed weakly. Note that although $\omega = \tilde{\omega}$ might hold at the continuous level, at the discrete level this equality does not hold in general. Below, the MEEVC discretisation for turbidity currents with kinematic Neumann boundary conditions is described.

4.2. MEEVC discretization for turbidity currents

Here, the modified MEEVC scheme with kinematic Neumann boundary conditions is adapted for the computation of the lock exchange flow presented in Section 3. The first step is to write (11) in the (\vec{u}, ω, p) formulation of the MEEVC scheme:

$$\begin{cases} \frac{\partial \vec{u}}{\partial t} + \omega \times \vec{u} + \nabla \bar{p} = -\frac{1}{\sqrt{\text{Gr}}} \nabla \times \omega + \phi \vec{e}_g, \\ \frac{\partial \omega}{\partial t} + \frac{1}{2} (\vec{u} \cdot \nabla) \omega + \frac{1}{2} \nabla \cdot (\vec{u} \omega) = \frac{1}{\sqrt{\text{Gr}}} \Delta \omega + \nabla \phi \times \vec{e}_g, \\ \frac{\partial \phi}{\partial t} + \frac{1}{2} (\vec{u}_p \cdot \nabla) \phi + \frac{1}{2} \nabla \cdot (\vec{u}_p \phi) = \frac{1}{\sqrt{\text{GrSc}^2}} \Delta \phi, \\ \nabla \cdot \vec{u} = 0, \end{cases} \quad (41)$$

where $\vec{u}_p = \vec{u} + u_s \vec{e}_g$ and the identity $\nabla \times (\phi \vec{e}_g) = \nabla \phi \times \vec{e}_g$ has been used. The convective term for the particle transport equation has been written in skew-symmetric form to conserve the quadratic mean $\langle \phi, \phi \rangle$ at the discrete level. Conservation of $\langle \phi, \phi \rangle$ enforces $\phi \geq 0$ over Ω at the discrete level.

The next step is the construction of a weak formulation. The velocity \vec{u} is sought in the function space $H_0(\text{div}, \Omega)$, defined by

$$H_0(\text{div}, \Omega) = \{ \vec{u} \in H(\text{div}, \Omega) \mid \vec{u} \cdot \vec{n} = 0 \text{ on } \partial\Omega \}, \quad (42)$$

such that $\vec{u} \cdot \vec{n} = 0$ is strongly imposed along $\partial\Omega$. On the other hand, the vorticity ω is assumed to be contained in the space $H_{(2,4)}(\text{curl}, \Omega)$, defined

$$H_{(2,4)}(\text{curl}, \Omega) = \{ \omega \in H(\text{curl}, \Omega) \mid \omega = 0 \text{ on } \Gamma_2 \cup \Gamma_4 \}. \quad (43)$$

The particle concentration ϕ is contained in the space of functions with square integrable gradients, $H(\text{grad}, \Omega)$. The boundary conditions, given by (18) and (19), must be imposed weakly by means of Neumann boundary conditions. After integrating by parts, the weak form of the particle transport equation is,

$$\begin{aligned} \left\langle \frac{\partial \phi}{\partial t}, \zeta \right\rangle + \frac{1}{2} \langle \nabla \cdot (\vec{u}_p \phi), \zeta \rangle - \frac{1}{2} \langle \phi, \nabla \cdot (\vec{u}_p \zeta) \rangle + \frac{1}{2} \int_{\partial\Omega} \zeta \phi (\vec{u}_p \cdot \vec{n}) \, d\Gamma = \\ = \frac{1}{\sqrt{\text{GrSc}^2}} \left[-\langle \nabla \phi, \nabla \zeta \rangle + \int_{\partial\Omega} \zeta (\nabla \phi \cdot \vec{n}) \, d\Gamma \right], \quad \forall \zeta \in H(\text{grad}, \Omega). \end{aligned} \quad (44)$$

The term $\nabla \phi \cdot \vec{n}$ is equal to zero along $\Gamma_2 \cup \Gamma_3 \cup \Gamma_4$. On the other hand, $\vec{u}_p \cdot \vec{n} = u_s \vec{e}_g \cdot \vec{n}$ will be zero along the lateral faces, $\Gamma_2 \cup \Gamma_4$. Finally, $\nabla \phi \cdot \vec{n} = -\sqrt{\text{GrSc}^2} \phi u_s (\vec{e}_g \cdot \vec{n})$ on Γ_1 . These relations imply that (44) can be written as follows

$$\begin{aligned} \left\langle \frac{\partial \phi}{\partial t}, \zeta \right\rangle + \frac{1}{2} \langle \nabla \cdot (\vec{u}_p \phi), \zeta \rangle - \frac{1}{2} \langle \phi, \nabla \cdot (\vec{u}_p \zeta) \rangle = \\ = -\frac{1}{\sqrt{\text{GrSc}^2}} \langle \nabla \phi, \nabla \zeta \rangle + \int_{\Gamma_1} \zeta \phi u_s (\vec{e}_g \cdot \vec{n}) \, d\Gamma - \frac{1}{2} \int_{\Gamma_1 \cup \Gamma_3} \zeta \phi u_s (\vec{e}_g \cdot \vec{n}) \, d\Gamma = \\ = -\frac{1}{\sqrt{\text{GrSc}^2}} \langle \nabla \phi, \nabla \zeta \rangle + \frac{1}{2} \int_{\Gamma_1} \zeta \phi u_s \, d\Gamma - \frac{1}{2} \int_{\Gamma_3} \zeta \phi u_s \, d\Gamma, \quad \forall \zeta \in H(\text{grad}, \Omega). \end{aligned} \quad (45)$$

The weak form of (41) can be written as

$$\left\{ \begin{array}{ll} \text{Find } \vec{u} \in H_0(\text{div}, \Omega), p \in L^2(\Omega), \omega \in H_{(2,4)}(\text{curl}, \Omega) \text{ and } \phi \in H(\text{grad}, \Omega) & \text{such that:} \\ \langle \frac{\partial \vec{u}}{\partial t}, \vec{v} \rangle + \langle \omega \times \vec{u}, \vec{v} \rangle - \langle \vec{p}, \nabla \cdot \vec{v} \rangle = -\frac{1}{\sqrt{\text{Gr}}} \langle \nabla \times \omega, \vec{v} \rangle + \langle \phi \vec{e}_g, \vec{v} \rangle, & \forall \vec{v} \in H_0(\text{div}, \Omega), \\ \langle \frac{\partial \omega}{\partial t}, \xi \rangle + \frac{1}{2} \langle (\vec{u} \cdot \nabla) \omega, \xi \rangle + \frac{1}{2} \langle \nabla \cdot (\vec{u} \omega), \xi \rangle = \\ -\frac{1}{\sqrt{\text{Gr}}} \langle \nabla \times \omega, \nabla \times \xi \rangle + \frac{1}{\sqrt{\text{Gr}}} \int_{\partial \Omega} \xi (\nabla \times \vec{\omega}) \times \vec{n} \, d\Gamma + \langle \nabla \phi \times \vec{e}_g, \xi \rangle, & \forall \xi \in H_{(2,4)}(\text{curl}, \Omega), \\ \langle \frac{\partial \phi}{\partial t}, \zeta \rangle + \frac{1}{2} \langle \nabla \cdot (\vec{u}_p \phi), \zeta \rangle - \frac{1}{2} \langle \phi, \nabla \cdot (\vec{u}_p \zeta) \rangle = \\ -\frac{1}{\sqrt{\text{GrSc}^2}} \langle \nabla \phi, \nabla \zeta \rangle + \frac{1}{2} \int_{\Gamma_1} \zeta \phi u_s \, d\Gamma - \frac{1}{2} \int_{\Gamma_3} \zeta \phi u_s \, d\Gamma, & \forall \zeta \in H(\text{grad}, \Omega), \\ \langle \nabla \cdot \vec{u}, q \rangle = 0, & \forall q \in L^2(\Omega). \end{array} \right. \quad (46)$$

The finite element discretization of (46) can be developed once a set of finite element spaces is chosen for the variables, these are extended in terms of the basis functions and a time integrator is implemented. Following the steps taken in the MEEVC scheme with kinematic Neumann boundary conditions and taking into account that the space CG_N is chosen for ϕ_h , the following algorithm is developed:

Given $\vec{u}_h^{k+\frac{1}{2}}, \omega_h^k$ and ϕ^k ,

Step 1. Find $\tilde{\omega}_h^{k+1} \in \text{CG}_{N,(2,4)} = \{\omega_h \in \text{CG}_N \mid \omega_h = 0 \text{ on } \Gamma_2 \cup \Gamma_4\}$ such that:

$$\langle \tilde{\omega}_h^{k+\frac{1}{2}}, \xi_h \rangle = \langle \vec{u}_h^{k+\frac{1}{2}}, \nabla \times \xi_h \rangle, \quad \forall \xi_h \in \text{CG}_{N,(2,4)}. \quad (47)$$

Step 2. Find $\phi_h^{k+1} \in \text{CG}_N$ such that:

$$\begin{aligned} & \langle \frac{\phi_h^{k+1} - \phi_h^k}{\Delta t}, \zeta_h \rangle + \frac{1}{2} \langle \nabla \cdot \left((\vec{u}_h^{k+\frac{1}{2}} + u_s \vec{e}_g) \frac{\phi_h^{k+1} + \phi_h^k}{2} \right), \zeta_h \rangle - \frac{1}{2} \langle \frac{\phi_h^{k+1} + \phi_h^k}{2}, \nabla \cdot \left((\vec{u}_h^{k+\frac{1}{2}} + u_s \vec{e}_g) \zeta_h \right) \rangle = \\ & -\frac{1}{\sqrt{\text{GrSc}^2}} \langle \nabla \left(\frac{\phi_h^{k+1} + \phi_h^k}{2} \right), \nabla \zeta_h \rangle + \frac{1}{2} \int_{\Gamma_1} \zeta_h \frac{\phi_h^{k+1} + \phi_h^k}{2} u_s \, d\Gamma - \frac{1}{2} \int_{\Gamma_3} \zeta_h \frac{\phi_h^{k+1} + \phi_h^k}{2} u_s \, d\Gamma, \quad \forall \zeta_h \in \text{CG}_N \end{aligned} \quad (48)$$

Step 3. Find $\omega_h^{k+1} \in \text{CG}_{N,(2,4)}$ such that:

$$\begin{aligned} & \langle \frac{\omega_h^{k+1} - \omega_h^k}{\Delta t}, \xi_h \rangle - \frac{1}{2} \langle \frac{\omega_h^{k+1} + \omega_h^k}{2}, \nabla \cdot (\vec{u}_h^{k+\frac{1}{2}} \xi_h) \rangle + \frac{1}{2} \langle \nabla \cdot \left(\vec{u}_h^{k+\frac{1}{2}} \frac{\omega_h^{k+1} + \omega_h^k}{2} \right), \xi \rangle = \\ & = -\frac{1}{\sqrt{\text{Gr}}} \langle \nabla \times \omega_h^{k+1}, \vec{v}_h \rangle + \frac{1}{\sqrt{\text{Gr}}} \int_{\partial \Omega} \xi_h (\nabla \times \vec{\omega}_h^{k+\frac{1}{2}}) \times \vec{n} \, d\Gamma + \langle \nabla \tilde{\phi}_h^{k+\frac{1}{2}} \times \vec{e}_g, \xi_h \rangle, \quad \forall \xi_h \in \text{CG}_{N,(2,4)}, \end{aligned} \quad (49)$$

with

$$\tilde{\phi}_h^{k+\frac{1}{2}} = \frac{\phi_h^{k+1} + \phi_h^k}{2}. \quad (50)$$

Step 4. Find $(\vec{u}_h^{k+\frac{3}{2}}, \vec{p}^{k+1}) \in (\text{RT}_{N,0}, \text{DG}_{N-1})$ such that:

$$\left\{ \begin{array}{ll} \langle \frac{\vec{u}_h^{k+\frac{3}{2}} - \vec{u}_h^{k+\frac{1}{2}}}{\Delta t}, \vec{v}_h \rangle + \langle \omega_h^{k+1} \times \frac{\vec{u}_h^{k+\frac{3}{2}} + \vec{u}_h^{k+\frac{1}{2}}}{2}, \vec{v}_h \rangle - \langle \vec{p}_h^{k+1}, \nabla \cdot \vec{v}_h \rangle = \\ -\frac{1}{\sqrt{\text{Gr}}} \langle \nabla \times \omega_h^{k+1}, \vec{v}_h \rangle + \langle \phi_h^{k+1} \vec{e}_g, \vec{v} \rangle, & \forall \vec{v}_h \in \text{RT}_{(N,0)}, \\ \langle \nabla \cdot \vec{u}_h^{k+\frac{3}{2}}, q_h \rangle = 0, & \forall q_h \in \text{DG}_{N-1}. \end{array} \right. \quad (51)$$

5. Energy balance

The progressive conversion of potential energy into kinetic energy is the main mechanism that drives a turbidity current. The fluid motion decays over time due to viscous dissipation and the gradual loss of mass due to sedimentation. In this section, the energy balance equations are derived at the continuous level in the way of [9, 19, 20, 25]. Subsequently, the degree to which the discrete counterpart of the energy balance holds is analyzed.

5.1. Conservation of energy at the continuous level

Denoting the potential energy by E_p and the viscous and sedimentation dissipation rates with ε_v and ε_s , the global energy equation of the flow is given by,

$$\frac{d}{dt} (\mathcal{K} + E_p) = -\varepsilon_v - \varepsilon_s. \quad (52)$$

An expression for the conservation of kinetic energy can be derived from the momentum equation in its weak formulation by specifying $\vec{v} = \vec{u}$, see (46), such that,

$$\frac{d\mathcal{K}}{dt} = -\frac{1}{\sqrt{\text{Gr}}} \langle \nabla \times \omega, \vec{u} \rangle + \langle \phi \vec{e}_g, \vec{u} \rangle. \quad (53)$$

The potential energy, in its non-dimensional form, is defined,

$$E_p = \int_{\Omega} \phi y \, d\Omega, \quad (54)$$

such that its time derivative of E_p is given by,

$$\frac{dE_p}{dt} = \int_{\Omega} \frac{D\phi}{Dt} y \, d\Omega + \int_{\Omega} \phi \frac{Dy}{Dt} \, d\Omega = \left\langle \frac{D\phi}{Dt}, y \right\rangle - \langle \phi, \vec{u} \cdot \vec{e}_g \rangle. \quad (55)$$

Given (55), the term $\langle \phi, \vec{u} \cdot \vec{e}_g \rangle$ in (53) can be written as a function of E_p . Therefore, the energy budget equation can be written as

$$\frac{d\mathcal{K}}{dt} + \frac{dE_p}{dt} = -\frac{1}{\sqrt{\text{Gr}}} \langle \nabla \times \omega, \vec{u} \rangle + \left\langle \frac{D\phi}{Dt}, y \right\rangle. \quad (56)$$

This equation yields an expression for the dissipation terms due to viscosity, denoted ε_v , and sedimentation, ε_s , such that,

$$\varepsilon_v = \frac{1}{\sqrt{\text{Gr}}} \langle \nabla \times \omega, \vec{u} \rangle, \quad (57)$$

$$\varepsilon_s = -\left\langle \frac{D\phi}{Dt}, y \right\rangle. \quad (58)$$

A simpler expression can be found for (58) that does not require derivation over time. In the particle transport equation, the advection velocity is $\vec{u}_p = \vec{u} + u_s \vec{e}_g$. Taking into account that u_s is constant, see (6), the particle transport equation takes the following form for $\zeta = y$,

$$\left\langle \frac{D\phi}{Dt}, y \right\rangle = -u_s \langle \nabla \phi \cdot \vec{e}_g, y \rangle - \frac{1}{\sqrt{\text{GrSc}^2}} \left(\langle \nabla \phi, \nabla y \rangle - \int_{\partial\Omega} y \nabla \phi \cdot \vec{n} \, d\Gamma \right). \quad (59)$$

The first term in (59) can be integrated by parts,

$$\begin{aligned} -u_s \langle \nabla \phi \cdot \vec{e}_g, y \rangle &= u_s \langle \phi, \nabla y \cdot \vec{e}_g \rangle - u_s \int_{\partial\Omega} \phi y (\vec{e}_g \cdot \vec{n}) \, d\Gamma \\ &= -u_s \langle \phi, 1 \rangle + 2u_s \int_{\Gamma_1} \phi \, d\Gamma, \end{aligned} \quad (60)$$

and, taking into account boundary conditions (18) and (19), the boundary term in (59) results in,

$$\frac{1}{\sqrt{\text{GrSc}^2}} \int_{\partial\Omega} y \nabla \phi \cdot \vec{n} \, d\Gamma = -2u_s \int_{\Gamma_1} \phi \, d\Gamma. \quad (61)$$

Therefore, (59) can be written as follows,

$$\left\langle \frac{D\phi}{Dt}, y \right\rangle = -u_s \langle \phi, 1 \rangle + \frac{1}{\sqrt{\text{GrSc}^2}} \langle \nabla \phi, \vec{e}_g \rangle, \quad (62)$$

such that ϵ_s corresponds with

$$\epsilon_s = u_s \langle \phi, 1 \rangle - \frac{1}{\sqrt{\text{GrSc}^2}} \langle \nabla \phi, \vec{e}_g \rangle. \quad (63)$$

The energy balance of a turbidity current is generally written in terms of time integrated values [9, 19, 20, 25]. Equation (53) can be written as follows,

$$\mathcal{K} + E_p + E_v + E_s = \mathcal{K}_0 + E_{p,0}, \quad (64)$$

where \mathcal{K}_0 and $E_{p,0}$ are the initial kinetic and potential energy and E_v and E_s are the total energy losses to viscous dissipation and suspended particles. E_v and E_s are given by

$$E_v = \int_0^t \epsilon_v \, d\tau \quad \text{and} \quad E_s = \int_0^t \epsilon_s \, d\tau. \quad (65)$$

5.2. Conservation of energy at the discrete level

A discrete energy balance equation, equivalent to (64), can be derived from the discretized equations of motion, given by (47) to (51). The discretized energy balance equation is constructed by imitating the derivation carried out in Section 5.1 and taking into account which steps and vector identities are exact at the discrete level.

A discrete statement of the conservation of kinetic energy can be written by setting $\vec{v}_h = \frac{1}{2}\vec{u}_h^{k+\frac{3}{2}} + \frac{1}{2}\vec{u}_h^{k+\frac{1}{2}}$ in the discrete momentum equation. In the same way as presented in Section ??, the following equation can be derived,

$$\frac{1}{2} \langle \vec{u}_h^{k+\frac{3}{2}}, \vec{u}_h^{k+\frac{3}{2}} \rangle - \frac{1}{2} \langle \vec{u}_h^{k+\frac{1}{2}}, \vec{u}_h^{k+\frac{1}{2}} \rangle = -\frac{\Delta t}{\sqrt{\text{Gr}}} \langle \nabla \times \omega_h^{k+1}, \frac{\vec{u}_h^{k+\frac{3}{2}} + \vec{u}_h^{k+\frac{1}{2}}}{2} \rangle + \Delta t \langle \phi^{k+1} \vec{e}_g, \frac{\vec{u}_h^{k+\frac{3}{2}} + \vec{u}_h^{k+\frac{1}{2}}}{2} \rangle. \quad (66)$$

The discrete kinetic energy \mathcal{K}_h^{k+1} is defined in (??). The discrete counterpart of ϵ_v is defined as,

$$\epsilon_{v,h}^{k+1} = \frac{1}{\sqrt{\text{Gr}}} \langle \nabla \times \omega_h^{k+1}, \frac{\vec{u}_h^{k+\frac{3}{2}} + \vec{u}_h^{k+\frac{1}{2}}}{2} \rangle. \quad (67)$$

Therefore, Equation (66) can be written as follows,

$$\mathcal{K}_h^{k+1} - \mathcal{K}_h^k = -\Delta t \, \epsilon_{v,h}^{k+1} + \Delta t \langle \phi^{k+1} \vec{e}_g, \frac{\vec{u}_h^{k+\frac{3}{2}} + \vec{u}_h^{k+\frac{1}{2}}}{2} \rangle. \quad (68)$$

The potential energy and the dissipation due to sedimentation can be introduced by using the discrete transport equation for the particle phase, Equation (48). To this end, the discrete test function is set to $\zeta_h = y$ and the convective terms are rewritten as follows,

$$\frac{1}{2} \langle \nabla \cdot \left(\vec{u}_h^{k+\frac{1}{2}} \frac{\phi_h^{k+1} + \phi_h^k}{2} \right), y \rangle - \frac{1}{2} \langle \frac{\phi_h^{k+1} + \phi_h^k}{2}, \nabla \cdot (\vec{u}_h^{k+\frac{1}{2}} y) \rangle = \langle \tilde{\phi}^{k+\frac{1}{2}}, \vec{u}_h^{k+\frac{1}{2}} \cdot \vec{e}_g \rangle, \quad (69)$$

$$\frac{1}{2} \langle \nabla \cdot \left(u_s \vec{e}_g \frac{\phi_h^{k+1} + \phi_h^k}{2} \right), y \rangle - \frac{1}{2} \left\langle \frac{\phi_h^{k+1} + \phi_h^k}{2}, \nabla \cdot (u_s \vec{e}_g y) \right\rangle + \frac{1}{2} \int_{\Gamma_1} y \frac{\phi_h^{k+1} + \phi_h^k}{2} u_s (\vec{e}_g \cdot \vec{n}) \, d\Gamma = -u_s \langle \tilde{\phi}_h^{k+\frac{1}{2}}, 1 \rangle, \quad (70)$$

where integration by parts has been applied on the first terms in both cases, an operation which is exact at the discrete level because $\nabla \cdot \vec{u}_h = 0$ and $\vec{u}_h \cdot \vec{n} = 0$. For simplicity of notation, $\tilde{\phi}^{k+\frac{1}{2}}$ is used, see (50). The discrete counterparts of E_p and ϵ_s are defined as,

$$E_{p,h}^k = \langle \phi_h^k, y \rangle, \quad (71)$$

$$\epsilon_{s,h}^k = u_s \langle \tilde{\phi}_h^k, 1 \rangle - \frac{1}{\sqrt{\text{GrSc}^2}} \langle \nabla \tilde{\phi}_h^k, \vec{e}_g \rangle, \quad (72)$$

such that (48) can be rewritten as follows,

$$E_{p,h}^{k+1} - E_{p,h}^k = -\Delta t \epsilon_{s,h}^{k+\frac{1}{2}} - \Delta t \left\langle \frac{\phi_h^{k+1} + \phi_h^k}{2} \vec{e}_g, \vec{u}_h^{k+\frac{1}{2}} \right\rangle. \quad (73)$$

A discrete energy balance equation analogous to (52) is obtained by summing (68) and (73),

$$\mathcal{K}_h^{k+\frac{3}{2}} + E_{p,h}^{k+1} = \mathcal{K}_h^{k+\frac{1}{2}} + E_{p,h}^k - \Delta t \left(\epsilon_{v,h}^{k+1} + \epsilon_{s,h}^{k+\frac{1}{2}} \right) + \frac{\Delta t}{2} \left(\langle \phi_h^{k+1} \vec{e}_g, \vec{u}_h^{k+\frac{3}{2}} \rangle - \langle \phi_h^k \vec{e}_g, \vec{u}_h^{k+\frac{1}{2}} \rangle \right). \quad (74)$$

The last term in (74) is a residual term due to the staggering in time of the momentum equation with respect to particle transport equation. The temporal evolution of the residual can be understood by deriving the integral form of (74). The following expressions are obtained at the time iterations $k, k-1, \dots, 1$ and 0 :

$$\begin{aligned} \mathcal{K}_h^{k+\frac{3}{2}} + E_{p,h}^{k+1} &= \mathcal{K}_h^{k+\frac{1}{2}} + E_{p,h}^k - \Delta t \left(\epsilon_{v,h}^{k+1} + \epsilon_{s,h}^{k+\frac{1}{2}} \right) + \frac{\Delta t}{2} \left(\langle \phi_h^{k+1} \vec{e}_g, \vec{u}_h^{k+\frac{3}{2}} \rangle - \langle \phi_h^k \vec{e}_g, \vec{u}_h^{k+\frac{1}{2}} \rangle \right), \\ \mathcal{K}_h^{k+\frac{1}{2}} + E_{p,h}^k &= \mathcal{K}_h^{k-\frac{1}{2}} + E_{p,h}^{k-1} - \Delta t \left(\epsilon_{v,h}^k + \epsilon_{s,h}^{k-\frac{1}{2}} \right) + \frac{\Delta t}{2} \left(\langle \phi_h^k \vec{e}_g, \vec{u}_h^{k+\frac{1}{2}} \rangle - \langle \phi_h^{k-1} \vec{e}_g, \vec{u}_h^{k-\frac{1}{2}} \rangle \right), \\ &\vdots \\ \mathcal{K}_h^{\frac{5}{2}} + E_{p,h}^2 &= \mathcal{K}_h^{\frac{3}{2}} + E_{p,h}^1 - \Delta t \left(\epsilon_{v,h}^2 + \epsilon_{s,h}^{\frac{3}{2}} \right) + \frac{\Delta t}{2} \left(\langle \phi_h^2 \vec{e}_g, \vec{u}_h^{\frac{5}{2}} \rangle - \langle \phi_h^1 \vec{e}_g, \vec{u}_h^{\frac{3}{2}} \rangle \right), \\ \mathcal{K}_h^{\frac{3}{2}} + E_{p,h}^1 &= \mathcal{K}_h^{\frac{1}{2}} + E_{p,h}^0 - \Delta t \left(\epsilon_{v,h}^1 + \epsilon_{s,h}^{\frac{1}{2}} \right) + \frac{\Delta t}{2} \left(\langle \phi_h^1 \vec{e}_g, \vec{u}_h^{\frac{3}{2}} \rangle - \langle \phi_h^0 \vec{e}_g, \vec{u}_h^{\frac{1}{2}} \rangle \right). \end{aligned}$$

The summation of all the energy balance equations from t^{k+1} to t^1 produces the following result,

$$\mathcal{K}_h^{k+\frac{3}{2}} + E_{p,h}^{k+1} = \mathcal{K}_h^{\frac{1}{2}} + E_{p,h}^0 - \Delta t \sum_{i=1}^{k+1} \left(\epsilon_{v,h}^i + \epsilon_{s,h}^{i-\frac{1}{2}} \right) + \frac{\Delta t}{2} \left(\langle \phi_h^{k+1} \vec{e}_g, \vec{u}_h^{k+\frac{3}{2}} \rangle - \langle \phi_h^0 \vec{e}_g, \vec{u}_h^{\frac{1}{2}} \rangle \right). \quad (75)$$

Given the discrete counterpart of the total dissipated energy,

$$E_{v,h}^{k+1} = \Delta t \sum_{i=1}^{k+1} \epsilon_{v,h}^i \quad \text{and} \quad E_{s,h}^{k+\frac{1}{2}} = \Delta t \sum_{i=1}^{k+1} \epsilon_{s,h}^{i-\frac{1}{2}}, \quad (76)$$

an integral energy balance equation for the discrete system can be derived,

$$\mathcal{K}_h^{k+\frac{3}{2}} + E_{p,h}^{k+1} + E_{v,h}^{k+1} + E_{s,h}^{k+\frac{1}{2}} = \mathcal{K}_h^{\frac{1}{2}} + E_{p,h}^0 + \frac{\Delta t}{2} \left(\langle \phi_h^{k+1} \vec{e}_g, \vec{u}_h^{k+\frac{3}{2}} \rangle - \langle \phi_h^0 \vec{e}_g, \vec{u}_h^{\frac{1}{2}} \rangle \right). \quad (77)$$

Equation (77) indicates that, due to staggering in time, a discrete statement for the conservation of energy cannot be exact because the different components of the energy are known at different time instants. The residual term of (77) is not a sink/source of energy because it is not accumulated over time, it quantifies the level of mismatch between the staggered variables in time. It is proportional only to Δt .

6. Numerical results

In this section, results are shown for the lock exchange test case described in Section 3. The objective of this section is to validate the modified MEEVC scheme and its robustness. In order to do so, 3 simulations are carried out with different levels of refinement and the results are compared with those given by Parkinson et al. [9] and Espath et al. [25].

In these computations, the Grashof and the Schmidt numbers are set to $\text{Gr} = 5 \times 10^6$ ($\text{Re} \approx 2236$) and $\text{Sc} = 1$. The simulations presented in the literature compute the flow problem up to $t = 60$ for a domain of length $L = 19$. The references used for the comparison, denoted Ref. 1 and Ref. 2 hereafter, are briefly explained below.

- **Ref. 1**, Parkinson et al. [9]. A mixed finite element method based on discontinuous Galerkin (DG) elements is used, with linear elements for \vec{u} and ϕ and quadratic elements for p . A Crank-Nicolson time discretization is used and the resulting non-linear system of equations is solved using two Picard iterations. Fixed and highly adaptive meshes are used. Unlike the boundary conditions presented in Section 3.1, $\phi = 0$ is prescribed along the top boundary, resulting in a loss of $< 1\%$ of mass and $\sim 3\%$ of the total energy.
- **Ref. 2**, Espath et al. [25]. A compact sixth-order finite difference scheme is used for the spatial discretization and a third order Adams-Bashforth scheme for time integration.

In total, 3 simulations are carried out with the modified MEEVC scheme; these are denoted by Sim 1, 2 and 3 and the discretization parameters can be found in Table 1. Due to the lack of available computing power (see Section ?? for details of the workstation), the simulations are computed from $t = 0$ to $t = 12$ and in a domain of length $L = 13$. At $t = 12$, the particle flow is far from reaching the opposite wall and the difference in domain length with the references should not modify the results. According to Härtel et al. [17], the propagating front remains unaffected by the wall up to a distance of $2H$, a condition satisfied in these computations.

In all of the simulations, the time step is set to $\Delta t = 10^{-3}$, following Espath et al. [25]. An “equivalent number of cells” is calculated in order to facilitate comparisons, defined

$$\text{eq. num. cells} = \text{num. cells} \times \frac{19}{13} \times N^2, \quad (78)$$

such that the domain is extended to $L = 19$ and the polynomial order is accounted for by triangulating each element into N^2 cells. The meshes used in the simulations are depicted in Figure 8.

Figure 8 displays the color plots of the particle concentration at $t = 4$ and 12, together with the corresponding meshes. Color plots from Parkinson et al. [9] are also shown because they illustrate the effects of mesh refinement and a mixed finite element method is also used. The first plot is a low resolution computation with a fixed mesh, while the second and third plots are high resolution computations with a fixed and an adaptive mesh, respectively. These last two plots are of approximately the same degree of accuracy [9].

The particle concentration fields obtained with the modified MEEVC scheme resemble the high resolution reference results for $t = 4$. For $t = 4$, an intrusion front has fully developed and a vortical structure,

Table 1: Discretization parameters of the three simulations carried out with the modified MEEVC scheme. The Grashof and the Schmidt numbers are set to $\text{Gr} = 5 \times 10^6$ and $\text{Sc} = 1$.

id	N	num. cells	eq. num. cells	Δt	d_W	d_U	d_Q
Sim 1	4	1116	2.6×10^4	10^{-3}	9169	20328	11160
Sim 2	4	2399	5.6×10^4	10^{-3}	19587	43576	23990
Sim 3	4	3599	8.4×10^4	10^{-3}	29283	65272	35990

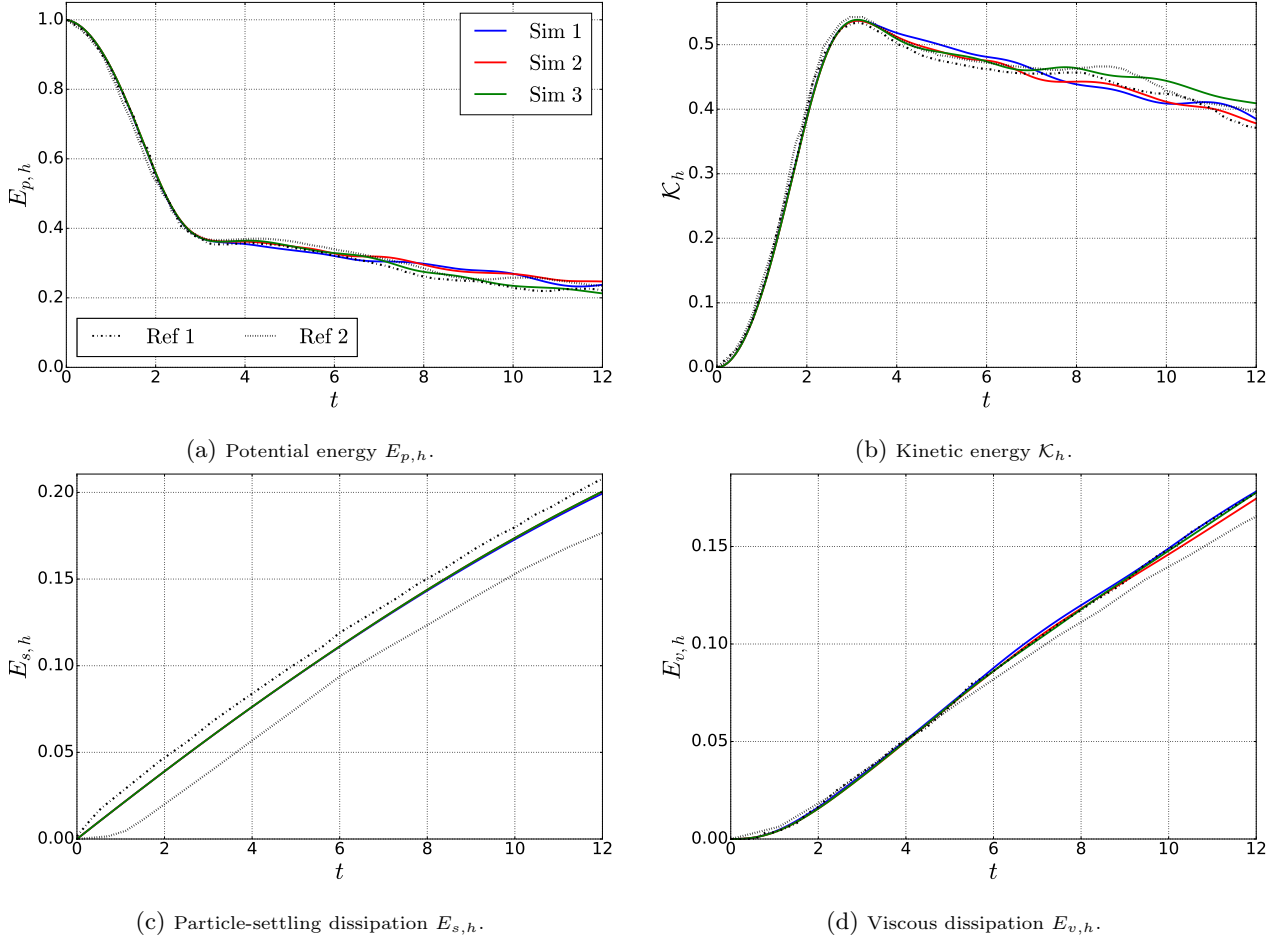


Figure 5: Variation over time of the 4 components of the energy balance equation. Results are compared with those of [9, 25].

characteristic of Kelvin-Helmholtz instabilities, are present along the upper interface. The reference results display two vortices along the upper interface, although for the low resolution case these are highly dissipated. With the MEEVC scheme these two vortices are captured, even with the lowest resolution. Interestingly, a third vortex appears in all of the MEEVC scheme computations. Possible differences could be due to the different ways in which boundary conditions are prescribed, to the highly dissipative nature of the reference scheme or to under resolved structures in the MEEVC scheme.

For $t = 12$, large variations appear from one computation to another. According to Parkinson et al. [9], no two simulations ever produced the same results. This is due to the highly chaotic nature of the flow; vortices are generated and propagated in such a way that small variations in the mesh induce small variations in these vortices which grow and propagate over time. However, in the two highly-resolved computations from the reference, three distinct vortical structures, suspended over the remains of the intrusion front, can be observed. These structures can also be observed in the three computations carried out with the MEEVC scheme. Considerable variations in the shape and position of these structures are found from Sim 2 to Sim 3. It must be taken into account that spatial convergence would require more computational power and it is not priority in this work.

In Figure 5, the evolution of the 4 discrete energy components can be found, see (64). The kinetic and potential energy are very similar for $t < 3$. Until $t = 6$, Sim 2 and 3 yield similar results. For $t > 6$, vortex interaction becomes stronger and the three simulations differ considerably. It can be concluded that, in general, good agreement can be found between the MEEVC computations and those of the references.

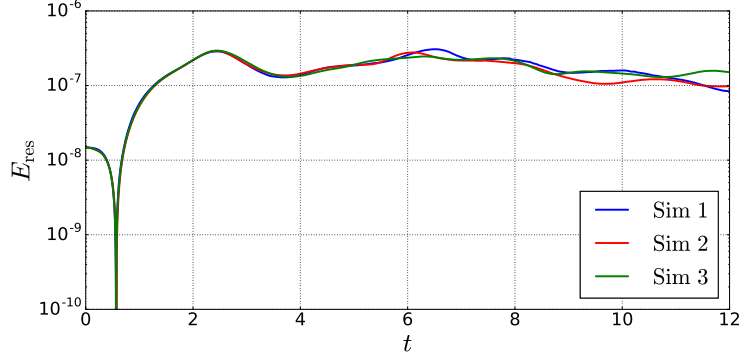


Figure 6: Energy residual E_{res} .

For the particle-settling dissipation, hardly no difference is found between the three MEEVC simulations. The values for $E_{s,h}$ given by the references differ from each other and from the MEEVC scheme along the entire computation. Parkinson et al. use different boundary conditions at the top wall and the two references use a different expression for ϵ_s . Although these are equivalent at the continuous level, the discrete expressions may differ. Parkinson et al. calculate ϵ_s with

$$\epsilon_{s,\text{ref } 1} = -u_s \langle \vec{e}_g, \nabla \phi \rangle - \frac{1}{\sqrt{\text{GrSc}^2}} \left\{ \langle \nabla \phi, \nabla y \rangle - \int_{\partial\Omega} y \nabla \phi \cdot \vec{n} \, d\Gamma \right\}, \quad (79)$$

and Espath et al. use,

$$\epsilon_{s,\text{ref } 2} = -u_s \langle \vec{e}_g, \nabla \phi \rangle + \frac{1}{\sqrt{\text{GrSc}^2}} \langle \Delta \phi, y \rangle. \quad (80)$$

A powerful advantage of the MEEVC scheme is the energy conserving properties. Figure 6 displays the evolution of the energy residual, E_{res} , defined,

$$E_{res}^k = \mathcal{K}_h^k + E_{p,h}^k + E_{v,h}^k + E_{s,h}^k - E_{p,h}^0 - \mathcal{K}^0, \quad (81)$$

where $\mathcal{K}_h^k = \frac{1}{2}(\mathcal{K}_h^{k+\frac{3}{2}} + \mathcal{K}_h^{k+\frac{1}{2}})$. As expected, this term remains stable and bounded to relatively small values, indicating a lack of artificial dissipation. This error is only due to the staggering in time of the velocity, see (77)¹.

Three of the main features of a turbidity current are the location of the front x_f , the mass of suspended particles m_p and the sedimentation rate \dot{m}_s . The evolution of these variables is shown in Figure 7, together with data from Espath et al. [25]. The calculated values for the location of the front and the total suspended mass agree with the reference results. This last variable is defined as

$$\frac{m_p}{m_{p,0}} = \frac{1}{m_{p,0}} \int_{\Omega} \phi \, d\Omega, \quad \text{with} \quad m_{p,0} = \int_{\Omega} \phi(t=0) \, d\Omega. \quad (82)$$

The variation of m_p , denoted \dot{m}_s , is defined as

$$\dot{m}_s = - \int_{\Gamma_3} \phi u_s \, d\Gamma, \quad (83)$$

see (3.1) for a derivation. Figure 7c indicates that the results from Sim 2 and 3 are in great agreement and that a similar tendency to that of the reference is obtained. On the other hand, the results from Sim 1 show a more chaotic behavior.

¹The expression given in (77) for the residual was not derived until a few days before the hand-in of this document. There was not enough time to repeat the simulations in order to gather the required data for the calculation of the residual and give a more precise proof.

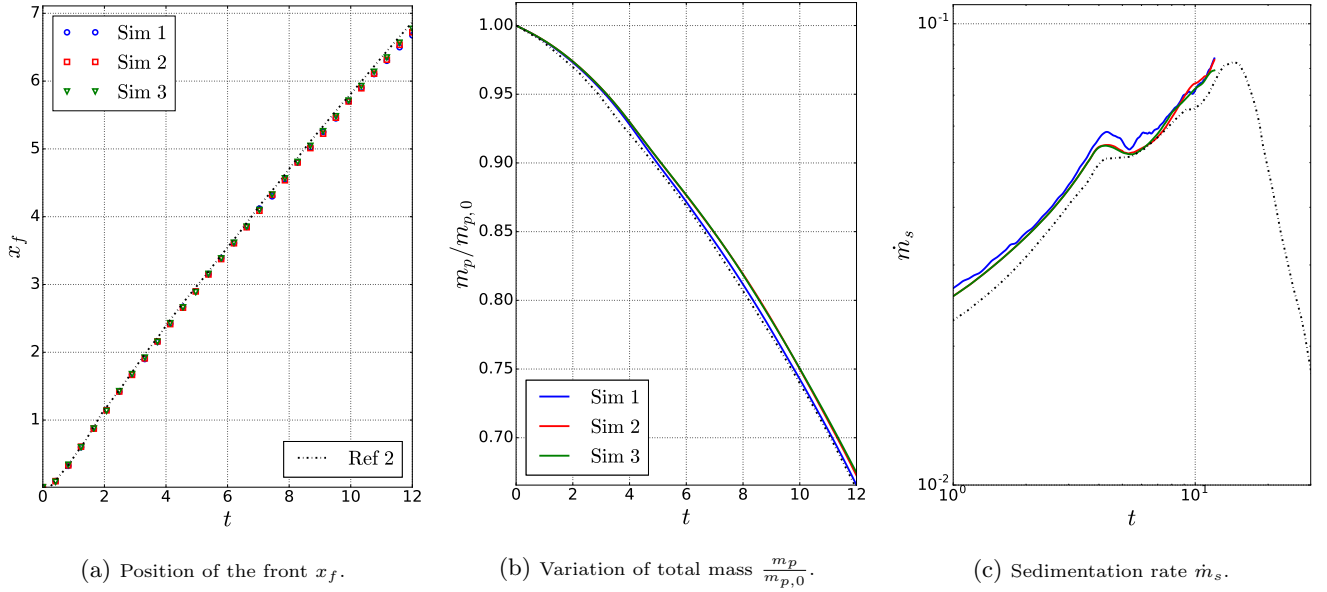


Figure 7: Variation over time of the location of the front, the suspended mass and the sedimentation rate. Comparisons are made with the results from [25].

7. Concluding remarks

In this chapter, a physics-compatible solver for turbidity currents is constructed from the MEEVC scheme with kinematic Neumann boundary conditions. It is proved that the discrete energy balance equation holds up to a residual which does not accumulate over time and is due to the staggering in time of the velocity. With the finite element basis functions used for the velocity and the pressure, $\nabla \cdot \vec{u}_h = 0$ over Ω and certain vector calculus identities required for the derivation of the energy balance equation hold at the discrete level. Essentially, the discrete kinetic and potential energy are only lost to the viscous and sedimentation terms, and no artificial dissipation of energy is introduced.

This solver is validated by computing the lock exchange test case for $Gr = 5 \times 10^6$ ($Re \approx 2236$) with three different meshes of increasing refinement. Comparisons are made with Parkinson et al. [9] and Espath et al. [25], and these indicate that the essential dynamics and vortical structures are captured with the lowest resolution. Further features of the flow are computed and compared with the reference results, showing very good agreement in general.

References

- [1] J. E. Simpson, Gravity Currents in the Laboratory, Atmosphere, and Ocean, *Annual Review of Fluid Mechanics* 14 (1982) 213–234.
- [2] M. Ungarish, An introduction to gravity currents and intrusions, CRC Press, 2009.
- [3] E. Meiburg, S. Radhakrishnan, M. Nasr-Azadani, Modeling gravity and turbidity currents: computational approaches and challenges, *Applied Mechanics Reviews* 67 (2015) 040802:1–23.
- [4] H. Huppert, Gravity currents: A personal perspective, *Journal of Fluid Mechanics* 554 (2006) 299–322.
- [5] E. Meiburg, B. Kneller, Turbidity Currents and Their Deposits, *Annual Review of Fluid Mechanics* 42 (2010) 135–156.
- [6] M. M. Nasr-Azadani, E. Meiburg, Turbidity currents interacting with three-dimensional seafloor topography, *Journal of Fluid Mechanics* 745 (2014) 409–443.
- [7] B. Kneller, W. McCaffrey, Depositional effects of flow nonuniformity and stratification within turbidity currents approaching a bounding slope; deflection, reflection, and facies variation, *Journal of Sedimentary Research* 69 (1999) 980–991.
- [8] J. Syvitski, C. Alexander, M. Field, J. Gardner, D. Orange, J. Yun, Continental-Slope Sedimentation: The View from Northern California, *Oceanography* 9 (1996) 163–167.
- [9] S. D. Parkinson, J. Hill, M. D. Piggott, P. A. Allison, Direct numerical simulations of particle-laden density currents with adaptive, discontinuous finite elements, *Geoscientific Model Development* 7 (2014) 1945–1960.

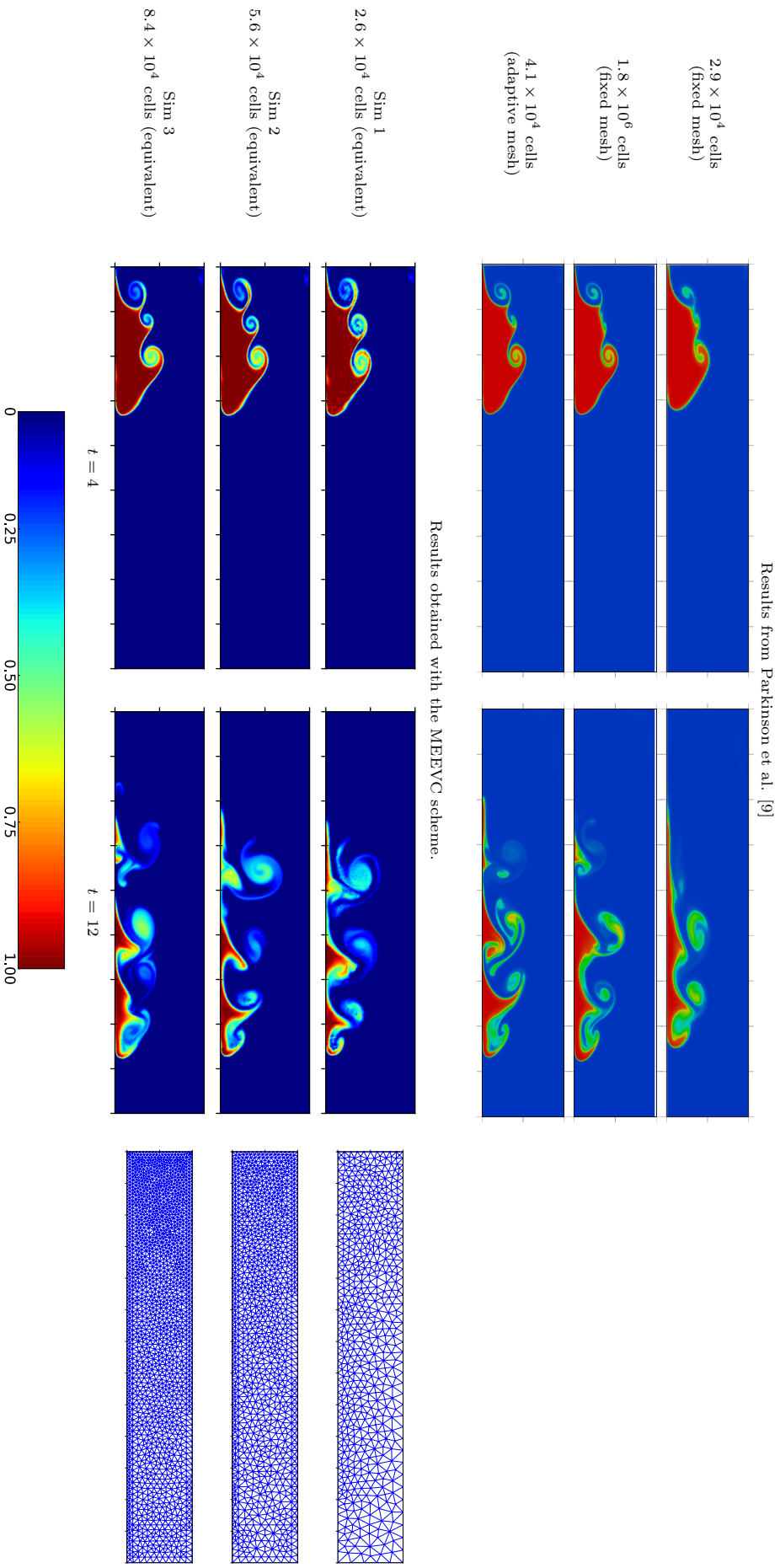


Figure 8: Distribution of particle concentration at $t = 4$ and 12 obtained with the three discretizations described in Table 1, together with the corresponding meshes. Three sets of results from [9] are also presented.

- [10] B. Kneller, C. Buckee, The structure and fluid mechanics of turbidity currents: a review of some recent studies and their geological implications, *Sedimentology* 47 (2000) 62–94.
- [11] T. von Kármán, The engineer grapples with non-linear problems, *Bulletin American Mathematical Society* 46 (1940) 615–683.
- [12] N. A. Konopliv, S. G. Llewellyn Smith, J. N. McElwaine, E. Meiburg, Modelling gravity currents without an energy closure, *Journal of Fluid Mechanics* 789 (2016) 806–829.
- [13] P. K. Kundu, I. M. Cohen, D. R. Dowling, *Fluid mechanics*, Academic Press, 2012.
- [14] P. R. Spalart, Strategies for turbulence modelling and simulations, *International Journal of Heat and Fluid Flow* 21 (2000) 252–263.
- [15] M. Lesieur, O. Metais, New Trends in Large-Eddy Simulations of Turbulence, *Annual Review of Fluid Mechanics* 28 (1996) 45–82.
- [16] Y. Zhiyin, Large-eddy simulation: Past, present and the future, *Chinese Journal of Aeronautics* 28 (2015) 11–24.
- [17] C. Härtel, L. Kleiser, M. Michaud, C. F. Stein, A direct numerical simulation approach to the study of intrusion flows, *Journal of Engineering Mathematics* 32 (1997) 103–120.
- [18] C. Härtel, E. Meiburg, F. Necker, Analysis and direct numerical simulation of the flow at a gravity-current head. part 1. flow topology and front speed for slip and no-slip boundaries, *Journal of Fluid Mechanics* 418 (2000) 189–212.
- [19] F. Necker, C. Härtel, L. Kleiser, E. Meiburg, High-resolution simulations of particle-driven gravity currents, *International Journal of Multiphase Flow* 28 (2002) 279–300.
- [20] F. Necker, C. Härtel, L. Kleiser, E. Meiburg, Mixing and dissipation in particle-driven gravity currents, *Journal of Fluid Mechanics* 545 (2005) 339–372.
- [21] F. Blanchette, M. Strauss, E. Meiburg, B. Kneller, M. E. Glinsky, High-resolution numerical simulations of resuspending gravity currents: Conditions for self-sustainment, *Journal of Geophysical Research* 110 (2005) C12022.
- [22] M. I. Cantero, S. Balachandar, M. H. Garcia, J. P. Ferry, Direct numerical simulations of planar and cylindrical density currents, *Journal of Applied Mechanics* 73 (2006) 923–930.
- [23] J. E. Birman, V. K. Martin, E. Meiburg, The non-boussinesq lock-exchange problem. part 2. high-resolution simulations, *Journal of Fluid Mechanics* 537 (2005) 125–144.
- [24] M. I. Cantero, S. Balachandar, M. H. Garcia, An eulerian-eulerian model for gravity currents driven by inertial particles, *International Journal of Multiphase Flow* 34 (2008) 484–501.
- [25] L. F. R. Espath, L. C. Pinto, S. Laizet, J. H. Silvestrini, Two- and three-dimensional direct numerical simulation of particle-laden gravity currents, *Computers and Geosciences* 63 (2014) 9–16.
- [26] A. Palha, M. I. Gerritsma, A mass, energy, enstrophy and vorticity conserving (MEEVC) mimetic spectral element discretization for the 2D incompressible Navier-Stokes equations, *Journal of Computational Physics* 328 (2017) 200–220.
- [27] G. G. de Diego, A. Palha, M. Gerritsma, Inclusion of no-slip boundary conditions in the MEEVC scheme, *Journal of Computational Physics* 378 (2019) 615–633.
- [28] J. Ferry, S. Balachandar, A fast Eulerian method for disperse two-phase flow, *International Journal of Multiphase Flow* 27 (2001) 1199–1226.
- [29] S. Elghobashi, On predicting particle-laden turbulent flows, *Applied Scientific Research* 52 (1994) 309–329.
- [30] S. Balachandar, A scaling analysis for point-particle approaches to turbulent multiphase flows, *International Journal of Multiphase Flow* 35 (2009) 801–810.
- [31] D. D. Joseph, T. S. Lundgren, R. Jackson, D. A. Saville, Ensemble averaged and mixture theory equations for incompressible fluidparticle suspensions, *International journal of multiphase flow* 16 (1990) 35–42.
- [32] J. E. Simpson, *Gravity Currents. In the environment and in the laboratory*, Cambridge University Press, 2nd edition, 1997.
- [33] T. A. Zang, On the rotation and skew-symmetric forms for incompressible flow simulations, *Applied Numerical Mathematics* 7 (1991) 27–40.
- [34] Y. Morinishi, T. Lund, O. Vasilyev, P. Moin, Fully conservative higher order finite difference schemes for incompressible flow, *Journal of Computational Physics* 143 (1998) 90–124.
- [35] E. M. Rønquist, Convection treatment using spectral elements of different order, *International Journal for Numerical Methods in Fluids* 22 (1996) 241–264.
- [36] T. B. Gatski, Review of incompressible fluid flow computations using the vorticity-velocity formulation, *Applied Numerical Mathematics* 7 (1991) 227–239.
- [37] O. Daube, Resolution of the 2D Navier-Stokes equations in velocity-vorticity form by means of an influence matrix technique, *Journal of Computational Physics* 103 (1992) 402–414.
- [38] H. Clercx, A spectral solver for the Navier-Stokes equations in the velocity-vorticity formulation for flows with two nonperiodic directions, *Journal of Computational Physics* 137 (1997) 186–211.
- [39] D. N. Arnold, R. S. Falk, R. Winther, Finite element exterior calculus: from Hodge theory to numerical stability, *Bulletin of the American Mathematical Society* 47 (2010) 281–354.
- [40] A. Palha, P. P. Rebelo, R. Hiemstra, J. Kreeft, M. I. Gerritsma, Physics-compatible discretization techniques on single and dual grids, with application to the Poisson equation of volume forms, *Journal of Computational Physics* 257 (2014) 1394–1422.
- [41] A. Bossavit, Computational electromagnetism and geometry: (1) Network equations, *Journal of the Japan Society of Applied Electromagnetics* 7 (1999) 150–159.
- [42] A. Bossavit, Computational electromagnetism and geometry: (2) Network constitutive laws, *Journal of the Japan Society of Applied Electromagnetics* 7 (1999) 294–301.
- [43] A. Bossavit, Computational electromagnetism and geometry: (3) Convergence, *Journal of the Japan Society of Applied*

- Electromagnetics 7 (1999) 401–408.
- [44] A. Bossavit, Computational electromagnetism and geometry: (4) From degrees of freedom to fields, *Journal of the Japan Society of Applied Electromagnetics* 8 (2000) 102–109.
 - [45] A. Bossavit, Computational electromagnetism and geometry: (5) The “Galerkin Hodge”, *Journal of the Japan Society of Applied Electromagnetics* 8 (2000) 203–209.
 - [46] C. Kirby, A. Logg, M. E. Rognes, A. R. Terrel, Common and unusual finite elements, in: *Automated Solution of Differential Equations by the Finite Element Method*, volume 84 of *Lecture Notes in Computational Science and Engineering*, Springer, 2012, pp. 95–119.
 - [47] P. Raviart, J. M. Thomas, A mixed finite element method for 2nd order elliptic problems, in: *Mathematical Aspects of the Finite Element Method*, volume 606 of *Lecture Notes in Mathematics*, Springer Berlin Heidelberg, 2006, pp. 292–315.
 - [48] E. Hairer, C. Lubich, G. Wanner, *Geometric numerical integration: structure-preserving algorithms for ordinary differential equations*, volume 31, Springer Science & Business Media, 2006.
 - [49] F. Brezzi, M. Fortin, *Mixed and Hybrid Finite Element Methods*, number 15 in Springer Series in Computational Mathematics 44, Springer, 1991.